

1 **Causes of interannual variability over the southern**
2 **hemispheric tropospheric ozone maximum**

3 Junhua Liu^{1,2}, Jose M. Rodriguez², Stephen D. Steenrod^{1,2}, Anne R. Douglass², Jennifer
4 A. Logan³, Mark Olsen^{2,4}, Krzysztof Wargan^{2,5}, Jerald Ziemke^{2,4}

5 ¹Universities Space Research Association (USRA), GESTAR, Columbia, MD, USA

6 ²NASA Goddard Space Flight Center, Greenbelt, Maryland, USA

7 ³School of Engineering and Applied Sciences, Harvard University, Cambridge, MA,
8 USA

9 ⁴Morgan State University, Baltimore, Maryland, USA

10 ⁵Science Systems and Applications, Inc., Lanham, MD, USA

11

12 *Correspondence to:* Junhua Liu (junhua.liu@nasa.gov)

13 **Abstract.**

14 We examine the relative contribution of processes controlling the interannual variability
15 (IAV) of tropospheric ozone over four sub-regions of the southern hemispheric
16 tropospheric ozone maximum (SHTOM) over a twenty-year period. Our study is based
17 on hindcast simulations from the National Aeronautics and Space Administration Global
18 Modeling Initiative – Chemistry transport model (NASA GMI-CTM) of tropospheric and
19 stratospheric chemistry, driven by assimilated Modern Era Retrospective-Analysis for
20 Research and Applications (MERRA) meteorological fields. Our analysis shows that over
21 SHTOM region, the IAV of the stratospheric contribution is the most important factor
22 driving the IAV of upper tropospheric ozone (270 hPa), where ozone has a strong
23 radiative effect. Over the south Atlantic region, the contribution from surface emissions
24 to the IAV of ozone exceeds that from stratospheric input at and below 430 hPa. Over the
25 south Indian Ocean, the IAV of stratospheric ozone makes the largest contribution to the
26 IAV of ozone with little or no influence from surface emissions at 270 hPa and 430 hPa
27 in austral winter. Over the tropical south Atlantic region, the contribution from IAV of
28 stratospheric input dominates in austral winter at 270 hPa and drops to less than half but
29 is still significant at 430 hPa. Emission contributions are not significant at these two
30 levels. The IAV of lightning over this region also contributes to the IAV of ozone in
31 September and December. Over the tropical southeastern Pacific, the contribution of the
32 IAV of stratospheric input is significant at 270 hPa and 430 hPa in austral winter, and
33 emissions have little influence.

34 **1 Introduction**

35 Tropospheric ozone plays a critical role in controlling the oxidative capacity of the
36 troposphere through its photolysis in the presence of water vapor, generating hydroxyl
37 radical (OH), the main atmospheric oxidant (e.g., Logan et al., 1981). It contributes to
38 smog and is harmful to human and ecosystem health near the surface. It acts as a
39 greenhouse gas especially in the upper troposphere (Lacis et al., 1990) and affects the
40 radiative forcing of the climate system. Tropospheric ozone is produced by
41 photochemical oxidation of CO and volatile organic compounds (VOCs) in the presence

42 of nitrogen oxides (NO_x) (e.g., Logan et al., 1981). Downward transport of ozone from
43 the stratosphere is also an important source of tropospheric ozone (e.g., Danielsen, 1968;
44 Stohl et al., 2003). Deep convection and long-range transport of ozone and its precursors
45 also modulate the tropospheric O_3 distributions (e.g., Chandra et al., 2009; Oman et al.,
46 2011).

47 Our study is motivated by the presence of tropospheric ozone maximum over tropical and
48 subtropical southern hemisphere as seen both in model simulations and GMAO
49 assimilated ozone product derived from OMI/MLS satellite measurements (Figure 1).
50 Although in the southern hemisphere tropospheric air is relatively “clean” and less
51 polluted compared with the Northern Hemisphere, this tropospheric ozone column
52 maximum reaches as high as 35DU and is comparable to the typical northern mid-latitude
53 values of 30DU. The elevated tropospheric ozone column is centered over the south
54 Atlantic from the equator to 30°S, and is part of the well-known tropical wave-one
55 pattern first noted in observations made by the Nimbus 7 Total Ozone Mapping
56 Spectrometer (TOMS) (e.g., Fishman et al., 1990; Ziemke et al., 1996). This ozone
57 maximum extends westward to South America and the tropical southeastern Pacific,
58 southeastward to southern Africa, south Indian Ocean along the latitude band of 30°S-
59 45°S, and is a dominant global feature (Thompson et al., 2003; Sauvage et al., 2007).
60 This elevated ozone region exists year-around, with a seasonal maximum in August -
61 October, and a seasonal minimum in April - May.

62 This study provides an examination of the relative contributions of the factors that control
63 the interannual variations of the southern hemisphere tropospheric ozone maximum over
64 a twenty-year period. Prior studies have examined the processes that produce the
65 southern hemisphere tropospheric ozone maximum (SHTOM), but consider only short
66 periods or are limited in spatial scale. These studies concluded that horizontal and vertical
67 transport of ozone precursors from regions of biomass burning (e.g., Jacob et al., 1996;
68 Thompson et al., 1996; Pickering et al., 1996; Jenkins and Ryu, 2004b; Sauvage et al.,
69 2006; Jourdain et al., 2007; Thouret et al., 2009), lightning NO_x (Martin et al., 2002;
70 Jenkins and Ryu, 2004a; Kim et al., 2013; Tocquer et al., 2015) and stratospheric
71 intrusions (Weller et al., 1996) all contribute to this tropospheric ozone column
72 maximum. However, changes of the relative contributions of these factors to tropospheric

73 ozone on inter-annual time scale over this region have not been examined in detail.
74 Studies considering tropospheric ozone interannual variability have not focused on the
75 SHTOM region. Hess and Mahowald (2009) used a CTM to quantify relative interannual
76 variability in global model ozone in hindcast simulations with constant emissions and
77 prescribed stratospheric ozone. The CTM was driven by two sets of meteorological
78 fields: a) the National Center for Environmental Prediction/National Center for
79 Atmospheric Research reanalysis; b) from a simulation using the Community
80 Atmosphere Model (CAM-3) forced with observed sea surface temperatures. Their study
81 found that relative IAV of ozone at 500 hPa shows the maximum between the Equator
82 and 30S in June-July-August (JJA) and December-January-February (DJF). Zeng and
83 Pyle (2005) used a climate/chemistry model to evaluate the ENSO effects on the
84 interannual variability of tropospheric ozone. Their study concludes that STE variation
85 induced by ENSO is one important factor driving the IAV of the global mean of
86 tropospheric ozone. Voulgarakis et al. (2010) examined the drivers of interannual
87 variability of the global tropospheric ozone using the p-TOMCAT tropospheric chemistry
88 transport model (CTM). Their study shows that changing transport including the STE is
89 important in determining the IAV of tropospheric ozone. Voulgarakis et al. (2011)
90 demonstrated that increases in the amounts of stratospheric ozone entering the
91 troposphere following El Niño events are mainly driven by changes in the STE. The
92 influence of emissions is confined to areas of intense burning on the interannual
93 timescale. Murray et al. (2013) examined the effects of lightning on the IAV in the
94 tropical tropospheric ozone column based on the GEOS-Chem CTM with IAV in tropical
95 lightning constrained by satellite observations from Lightning Imaging Sensors (LIS).
96 Their study finds that lightning plays an important role in driving the IAV of tropical
97 tropospheric ozone column, especially over East Africa, central Brazil, and in continental
98 outflow in the eastern Pacific and the Atlantic, but their model does not reproduce the
99 IAV in TCO except in East Africa and central Brazil. Liu et al. (2016) analyzed
100 simulations from a global chemistry and transport model to show that the IAV in the
101 stratospheric contribution significantly affects the IAV of upper tropospheric ozone at the
102 SHADOZ station over Reunion (21° S). In this study, we focus on the SHTOM region
103 and quantify the relative contributions of several factors to the tropospheric ozone

104 interannual variability during the past twenty years. We examine the horizontal and
105 vertical variations of these contributions by separating the SHTOM into four subregions
106 and comparing their IAVs at two selected levels (270 hPa and 430 hPa). This analysis
107 distinguishes between anthropogenic and natural sources on the IAV of the tropospheric
108 ozone and their contributions to the radiative forcing changes.

109 In this study, we use a global chemistry transport model to identify the processes
110 impacting observed interannual variability of the tropospheric ozone column maximum in
111 southern hemisphere. We examine the model sensitivity of tropospheric ozone to
112 different ozone sources through the use of multiple linear regression. We include
113 stratospheric input and emissions as two major predictor variables in our regression. We
114 include the lightning NO_x as the third factor in our regression model over the tropical
115 south Atlantic region, where ozone is sensitive to the IAV of lightning NO_x as found in
116 Murray et al (2013). In our multiple linear regression, a regression coefficient that is
117 significantly different from zero at the 95% confidence level implies that the
118 corresponding process contributes significantly to the variation of simulated ozone. To
119 estimate the variance explained by each predictor, we first calculate the sequential sums
120 of squares over ordering of predictors (see supplementary materials). The sequential of
121 squares depends on the predictors already in the model; we therefore do the calculation
122 for every possible order in which predictors can enter the model. We then average all the
123 sequential sums of squares to yield an adjusted sum of squares (Kruskal, 1987; Chevan
124 and Sutherland, 1991; Groemping, 2007). This method accounts for the likely possibility
125 that the two predictors are not orthogonal. We use the adjusted sum of squares to quantify
126 the relative contributions of each predictor to the interannual variability of tropospheric
127 ozone. Our study focuses on austral winter season when the subtropical jet related
128 stratosphere - troposphere exchange reaches the seasonal maximum (Karoly et al., 1998;
129 Bals-Elsholz et al., 2001; Nakamura and Shimpo, 2004). Southern hemisphere biomass
130 burning (e.g., Liu et al., 2010; 2013) also reaches the maximum during this season.

131 Section 2 briefly describes the model and simulations, including the standard chemistry
132 simulation, the stratospheric O_3 tracer simulation, and the tagged CO simulation. It also
133 describes GEOS-5 ozone assimilation, as the assimilated fields are used to evaluate
134 model performance over the southern hemisphere extra-tropics and tropics as discussed

135 in the first part of Section 3. The second part of Section 3 presents a diagnostic study of
136 controlling factors, including stratosphere input, surface emissions and lightning, on the
137 tropospheric ozone IAV relying on a series of hindcast simulations from 1992 to 2011.
138 Section 4 is a summary and conclusion.

139 **2 Model and Data**

140 **2.1 Model**

141 We used the Global Modeling Initiative chemical transport model (GMI-CTM) (Duncan
142 et al., 2007; Strahan et al., 2007), driven by MERRA reanalysis meteorology (Rienecker
143 et al., 2011, <http://gmao.gsfc.nasa.gov/research/merra/>). The native resolution of the
144 MERRA field is $0.67^{\circ} \times 0.5^{\circ}$ with 72 vertical levels; we regrid it to $2^{\circ} \times 2.5^{\circ}$ horizontal
145 grid for input to the GMI-CTM simulations in this study.

146 The chemical mechanism used in GMI-CTM represents stratospheric and tropospheric
147 chemistry with offline aerosols input from GOCART model simulations (Chin et al.,
148 2002). The GMI-CTM hindcast simulation has been used and compared to observations
149 in many recent studies. Strahan et al. (2013) showed excellent agreement between
150 simulated and MLS ozone profiles in the Arctic lower stratosphere. Liu et al. (2016)
151 shows the GMI-CTM hindcast and ozonesonde agree very well on the annual cycles and
152 IAV over Reunion from lower troposphere to the upper troposphere. Strode et al. (2015)
153 shows that the GMI-CTM hindcast reproduces the seasonal cycle and IAV of observed
154 surface ozone over United States from Environmental Protection Agency (EPA)'s Clean
155 Air Status and Trends Network (CASTNET).

156 The GMI-CTM standard simulation (labeled as Hindcast-VE) used in this study for 1992-
157 2011 includes monthly and inter-annually varying emissions with anthropogenic, biomass
158 burning, and biogenic sources. Anthropogenic emissions are based on the EDGAR 3.2
159 Inventory (Olivier et al., 2005), overwritten with available regional inventories for North
160 America, Europe, Asia and Mexico. More details are given in Strode et al. (2015).
161 Biomass burning emissions are from the Global Fire Emission Database, GFED3 (van
162 der Werf et al., 2010). Emission before 1997 are obtained from GFED3 emission
163 climatology averaged for 2001 to 2009 applied with regional-scale IAV, which was

164 derived from satellite information on fire activity (ATSR) and/or aerosol optical depths
165 from the Total Ozone Mapping Spectrometer (TOMS) by Duncan et al. (2003). Biogenic
166 emissions of isoprene and monoterpenes follow the latest version of the MEGAN
167 algorithm (Guenther et al., 2006). Besides the standard simulation, we carry out a control
168 run for 1991-2011 by repeating the anthropogenic and biomass emissions for 2000. The
169 comparison between the control and standard simulation removes the possible impact of
170 IAV in meteorology and allows us to quantify effects of emission IAV on ozone IAV.

171 In our GMI-CTM, the lightning parameterization follows the scheme described by Allen
172 et al (2010). The regional lightning NO_x emission, calculated online by coupling to the
173 deep convective transport in the model, varies from year to year. The global total of NO_x
174 from lightning is fixed at 5.0 TgN/yr.

175 Methane mixing ratios are specified in the two lowest model levels, using time dependent
176 zonal means from National Oceanic and Atmospheric Administration / Global
177 Monitoring Division (NOAA/GMD). Other long-lived source gases important in the
178 stratosphere, such as N_2O , CFCs, halocarbons are prescribed at the two lowest model
179 levels following the A2 scenario by (WMO, 2014). Stratospheric aerosol
180 distributions/trends are from International Global Atmospheric Chemistry/Stratospheric
181 Processes And their Role in Climate (IGAC/SPARC) and have IAV (Eyring et al., 2013).

182 The model includes a stratospheric O_3 tracer (Strat O_3). The Strat O_3 is defined relative to a
183 dynamically varying tropopause tracer (e90) (Prather et al., 2011). The e90 tracer is set to
184 a uniform mixing ratio (100 ppb) at the surface with 90 days e-folding lifetime. In our
185 simulation, the e90 tropopause value is 75 ppb. The Strat O_3 tracer is set equal to O_3 in the
186 stratosphere and is removed in the troposphere with the same loss frequency (chemistry
187 and deposition) archived from daily output of the standard chemistry model simulation
188 with yearly-varied emission in this study. Using the Strat O_3 tracer allows quantification
189 of O_3 of stratospheric origin in the troposphere at a given location and time. This
190 approach has also been adopted in the high resolution GFDL AM3 model (Lin et al.,
191 2012).

192 In this study, we also conducted a tagged CO simulation to examine the emission sources
193 during the same period as the full chemistry simulation. The tagged CO simulation has

194 horizontal resolution of $1^\circ \times 1.25^\circ$. The primary chemical loss of CO is through reactions
195 with OH radicals, which are archived from the respective standard chemistry simulation
196 with yearly-varied emissions. The chemical production and loss rates of CO in the
197 stratosphere were archived from the respective standard chemistry simulations.

198 **2.2 GMAO GEOS-5 Ozone Assimilation**

199 We used assimilated tropospheric ozone to evaluate model performance. This assimilated
200 dataset is produced by ingesting OMI v8.5 total column ozone and MLS v3.3 ozone
201 profiles into a version of the Goddard Earth Observing System, Version 5 (GEOS-5) data
202 assimilation system (Rienecker et al., 2011). No ozonesonde data are used in the
203 assimilation. Wargan et al. (2015) provides details of the GEOS-5.7.2 assimilation
204 system, which for this application is produced with $2^\circ \times 2.5^\circ$ horizontal resolution and
205 with 72 vertical layers between the surface and 0.01 hPa. For the troposphere, the
206 assimilation only applies a dry deposition mechanism at the surface without any chemical
207 production or loss. This algorithm works since the ozone lifetime is much longer than the
208 six-hour analysis time on which the background field is corrected by observations.
209 Ziemke et al. (2014) evaluated the tropospheric ozone profiles derived from three
210 strategies based on OMI and MLS measurements, including this GEOS-5 assimilation,
211 trajectory mapping and direct profile retrieval using residual method, with ozonesonde
212 observations and GMI model simulations. They show that the ozone product (500 hPa to
213 tropopause) from the GEOS-5 assimilation is the most realistic. Wargan et al. (2015) also
214 demonstrate that the ozone between 500 hPa and the tropopause from GEOS-5
215 assimilation is in good agreement with independent observations from ozonesondes. The
216 assimilation applies the OMI averaging kernels in the troposphere, but the weight of OMI
217 kernels decreases sharply below 500 hPa (Personal communication with K. Wargan).
218 Considering that in the lower troposphere there is no direct observational constraint in
219 the analysis, we use ozone mixing ratio at 270 hPa and 430 hPa as well as partial column
220 ozone integrated from 500 hPa to the tropopause from GEOS-5 assimilation as a
221 reference value to evaluate our GMI model simulation. To compare the GEOS-5
222 assimilated tropospheric partial column above 500 hPa with GMI-CTM ozone

223 simulation, we use the same tropopause as defined by the lower of the 3.5 potential
224 vorticity units (PVU) isosurface and the 380 K isentropic surface.

225 **3 Results**

226 **3.1 Temporal and spatial distribution of SHTOM in GMI-CTM and GMAO GEOS- 227 5 assimilated ozone product**

228 Figure 1 shows the spatial pattern of southern hemispheric partial column ozone (from
229 500 hPa to the tropopause) in four seasons averaged over 2005 to 2011 from the GMAO
230 GEOS-5 assimilated dataset and the GMI-CTM hindcast simulations. To account for a
231 low bias in the GEOS-5 ozone product (Wargan et al., 2015), we added 2.5 DU to the
232 assimilated column in the tropics (0-30°S). The GMI-CTM simulation reproduces the
233 seasonality and spatial distribution of southern hemispheric ozone maximum as shown in
234 GEOS-5 assimilated product with a) the elevated ozone centered over the Atlantic Ocean
235 from the equator to 40°S; b) the ozone maximum extending southeastward to southern
236 Africa and the Indian Ocean in the latitude band of 30°S-45°S; c) the relatively weaker
237 enhancement extending westward to South America and the tropical southeastern Pacific.
238 The ozone maximum is strongest in austral winter-spring and weakest in austral fall. Both
239 GMI-CTM and GEOS-5 assimilation show the very low tropospheric ozone over the
240 western Pacific and the tropical eastern Indian Ocean, where the ozone - poor marine
241 boundary layer air is lifted into the upper troposphere (Folkins et al., 2002; Solomon et
242 al., 2005).

243 **3.2 Subregions of SHTOM**

244 The tropospheric ozone distribution in any region depends on the advection and mixing,
245 its proximity to the polluted area, and descent of ozone-rich air from the stratosphere. We
246 show in Figure 2 the maps of simulated O_3 and $StratO_3/O_3$ at 430 hPa averaged over 1992
247 to 2011 in September, when the southern hemisphere biomass burning peaks. The
248 $StratO_3/O_3$ ratio represents the fraction of tropospheric ozone from the stratosphere and is
249 used to identify the regions with distinct stratospheric input. Differences in the spatial

250 patterns of the maximum/minimum in ozone mixing ratio and $\text{StratO}_3/\text{O}_3$ ratio identifies
251 regions where ozone is affected by factors other than the stratospheric input.
252 The region with minimum stratospheric ozone contribution occurs along the equator. In
253 the tropics, the southward extension of regions with minimum stratospheric ozone
254 contribution shows zonal variation, reaching 5°S to 10°S over tropical eastern Pacific and
255 tropical Atlantic, and further south to approximately 15°S over the Indian Ocean and the
256 Maritime Continents, which is closely related to the Walker Circulation. In this tropical
257 zonal circulation air rises over the Maritime Continents (together with deep convection)
258 and descends over the eastern Pacific (Bjerknes, 1969). Similar zonal circulation is found
259 over the Atlantic with rising due to radiative heating over tropical Africa and South
260 America and sinking due to radiative cooling over the tropical Atlantic (Julian and
261 Chervin, 1978). The longitudinal variation of ozone at 430 hPa in the tropics is in
262 agreement with the changes of $\text{StratO}_3/\text{O}_3$, showing ozone minimum over Maritime
263 Continents as well as elevated ozone over eastern Pacific and Atlantic. Within the
264 Atlantic, despite the smaller stratospheric contribution, the tropics have higher ozone
265 mixing ratio (>80 ppb) than the subtropics at 430 hPa, and other sources must also
266 contribute to the ozone maximum over tropical south Atlantic. Ozone over the tropical
267 southeastern Pacific is also slightly elevated. The maximum stratospheric influence is
268 found over the southern Indian and Pacific Oceans centered on 30°S, co-located with the
269 tropospheric O_3 maximum over these regions. Both ozone and $\text{StratO}_3/\text{O}_3$ over the
270 subtropics show strong longitudinal variations, with the co-located maxima over the
271 south Indian Ocean. The ozone minimum at 430 hPa at 30°S occurs over the eastern
272 Pacific region, while the minimum contribution of the stratospheric input is over the
273 south Atlantic region. Given the spatial variations of the maximum/minimum in
274 $\text{StratO}_3/\text{O}_3$ ratio and ozone mixing ratio, we separate the southern hemispheric ozone
275 maximum into four sub-regions: 1) Tropical southeastern Pacific (0-20°S, 150°W-60°W);
276 2) Tropical South Atlantic (0-15°S, 60°W-40°E); 3) Subtropical South Atlantic (15°S-
277 45°S, 60°W-40°E); 4) Subtropical South Indian Ocean (15°S-45°S, 40°E-150°E). We
278 show in Figure 3 the maps of the IAV of simulated O_3 at 270 hPa and 430 hPa. The IAV
279 is represented by the standard deviation of ozone anomalies (removing the monthly mean
280 averaged from 1992 to 2011) over 1992-2011. Relatively stronger ozone IAV happens

281 over subtropical south Atlantic and subtropical south Indian Ocean at 270 hPa. At 430
282 hPa, Tropical southeastern Pacific and tropical South Atlantic has slightly larger IAV. In
283 this paper, we examine and quantify the relative roles of dynamics and chemistry on the
284 IAV of tropospheric ozone variations over these selected regions during the past twenty
285 years.

286

287 Figure 4 compares the anomalies of modeled and assimilated upper tropospheric ozone
288 columns (UTOOC, integrated from 500 hPa to the tropopause) as well as the anomalies of
289 corresponding tropospheric ozone mixing ratio at 270 hPa and 430 hPa over two tropical
290 sub-regions (tropical south Atlantic and tropical southeastern Pacific) from 2005 to 2011.
291 The anomalies are calculated by removing the monthly mean averaged from 2005 to
292 2011. The short time scale variations in the model simulation tend to be greater compared
293 to that in the assimilated ozone products, especially over the tropical south Atlantic
294 region. But in general, the GMI-CTM hindcast simulation captures the assimilated IAV
295 of the tropospheric ozone at these two levels as well as for the UTOOC. Over the tropical
296 south Atlantic, the modeled IAV agrees with the phase changes of assimilated ozone IAV
297 but the simulation overestimates the assimilated ozone maximum in 2010 and
298 underestimates the assimilated minima in 2007 and 2011 at both levels. Over the tropical
299 southeastern Pacific, the IAV is influenced by ENSO related changes in dynamics (e.g.,
300 Ziemke et al., 2010;2011; Oman et al., 2013). The simulation reproduces much of the
301 assimilated IAV, showing high ozone anomalies after 2005, 2010 La Nina year and
302 negative ozone anomalies after strong El Niño year in 2009. However, during October
303 2006 to January 2007, the simulation shows a pronounced ozone peak, especially at 270
304 hPa, which is not seen in the assimilated ozone. Logan et al. (2008) examined interannual
305 variations of tropospheric ozone profiles in October-December between 2005 and 2006
306 based on the satellite observations from Tropospheric Emission Spectrometer (TES). The
307 TES data agree with what we found in the GMI-CTM model simulation, showing ozone
308 enhancement over the tropical southeastern Pacific (150°W-60°W, 0-12°S) region in
309 November 2006 relative to 2005 (~5-10 ppb at 250 hPa and 0-5 ppb at 400 hPa, Figure 3
310 of Logan et al., 2008). The agreement between TES and GMI-CTM indicates a possible
311 low bias of GMAO assimilated ozone during late 2006, as a result of the low sensitivity

312 of OMI (Wargan et al., 2015).
313 Figure 5 shows the similar comparison as Figure 4, but over the two subtropical regions.
314 Over the South Atlantic region, the assimilated ozone has similar but stronger IAV than
315 that over the tropical southeastern Pacific region, showing the largest ozone year-by-year
316 variation (~ 20 ppb at 270 hPa) from October 2009 to October 2010, and the GMI-CTM
317 simulation reproduces this variation quite well. Over the South Indian region, our model
318 reproduces most of the variations in magnitude and phase, but shows anti-phase
319 variations in late 2006/early 2007, which substantially affected the calculated correlation
320 coefficients between model and assimilated ozone. The simulated upper tropospheric
321 ozone column reproduces well the IAV in the assimilated ozone column except for the
322 late 2006. In general, agreement between the simulated and assimilated results confirms
323 the suitability of the model for investigations of the controlling factors on the
324 tropospheric ozone IAV over these regions.

325 The left column of Figure 6 presents the monthly profiles of correlation coefficients
326 between the simulated ozone and StratO₃ over the four sub-regions. Strong positive
327 correlations between StratO₃ and O₃ are observed in most seasons in the upper
328 troposphere even over two tropical regions. Stratospheric influence plays a big role
329 during austral winter-spring and reaches its seasonal maximum in August, when the
330 subtropical jet system is strongest and moves to its northern-most location. Over the two
331 subtropical regions, the strong stratospheric influence persists throughout the whole
332 troposphere ($r > 0.8$ at 700 hPa) in August. Over tropical south Atlantic region, the
333 strong stratospheric influence is limited to the upper troposphere in austral winter-spring
334 and decreases sharply with decreasing altitude. Over the tropical southeastern Pacific, the
335 strong stratospheric influence persists year-long at the upper troposphere and reaches as
336 low as ~ 400 hPa except for December.

337 The right column of Figure 6 shows the seasonal profiles of correlation coefficients
338 between ozone and ozone from emissions (EmissO₃). The EmissO₃ is the difference
339 between the simulations with varied and constant emission. Over the two subtropical
340 regions, there are two seasonal maxima in the correlations between ozone and EmissO₃.
341 The first occurs in September at the lower troposphere and decreases with increasing
342 altitude, the second is in December/January showing opposite vertical gradient with

343 stronger correlations in the upper and middle troposphere. Over the tropical southeastern
344 Pacific region, the influence from emissions shows a similar double-peak pattern, but
345 with the first maximum localized at the surface and the second peak localized in the
346 upper troposphere. Over the tropical south Atlantic, the influence of emissions is very
347 small. South America and southern Africa are two major nearby burning regions.
348 Emissions over South America have much larger IAV than those over southern Africa,
349 although African emissions are larger in absolute terms (Sauvage et al., 2007; Liu et al.,
350 2010; Voulgarakis et al., 2015). Sauvage et al (2007) argued that emissions over South
351 and Southeast Asia could be transported southward in the upper troposphere through the
352 Tropical Easterly Jet and affect ozone over Africa, the Atlantic and Indian Ocean
353 (Hoskins and Rodwell, 1995; Rodwell and Hoskins, 2001). Meanwhile, emissions over
354 this region also show large IAV (Voulgarakis et al., 2015). Therefore, the interannual
355 emission changes in South America (0-20°S, 72.5°W-37.5°W), southern Africa (5°S-
356 20°S, 12°E-38°E) and South and Southeast Asia (70°E-125°E, 10°S-40°N) may all affect
357 the IAV of ozone due to emission changes in the southern hemisphere. In this study, we
358 rely on tagged CO simulation to quantify the influence of biomass burning emissions
359 from these three burning regions during months when emission IAV contributes
360 significantly to the IAV of ozone.

361 In the next section, we choose August (the seasonal maximum of stratospheric input into
362 the lower troposphere), September and December (the seasonal maximum of emission
363 contribution) as three example months to examine the relative roles of different factors on
364 IAV of tropospheric ozone over these regions.

365 **3.3 Factors controlling IAV in ozone in the middle and upper troposphere**

366 **3.3.1 South Atlantic Region**

367 Figure 7 shows the multiple regression results over the South Atlantic region. It compares
368 the simulated ozone anomalies to that calculated from two regression variables: StratO₃
369 and EmissO₃ at 270 hPa and 430 hPa in August, September and December. The fitted
370 ozone anomalies in generally reproduce the IAV obtained from the GMI-CTM
371 simulation. The explained proportion of variability in simulated ozone anomalies by

372 StratO₃ and EmissO₃ is mostly above 50% and reaches as high as ~ 76% in December, at
373 270 hPa, which demonstrates that StratO₃ and EmissO₃ are sufficient to explain the IAV
374 of tropospheric ozone over the south Atlantic region. In August at 430 hPa, the fitted
375 ozone anomalies have a slightly weaker correlation with the simulated ozone and show
376 less IAV compared to the ozone anomalies in GMI-CTM.

377 Figure 8 exhibits regression results in a way that highlights the relative contributions of
378 the IAV of stratospheric input and emission on the IAV of ozone over South Atlantic.
379 The three panels represent results from August, September and December from 1992 to
380 2011. Each panel has two columns, which illustrate the respective contribution from
381 changes in StratO₃ and EmissO₃ on the IAV of ozone mixing ratio. The left column of
382 each panel compares the anomalies of StratO₃ (blue) and simulated ozone mixing ratio
383 (black) from the GMI-CTM model at 270 and 430 hPa. The right column compares the
384 simulated O₃ residual after removing the regression from StratO₃ (black line) and
385 EmissO₃ (green line) at these two levels. The regression coefficient (β) and its 95%
386 confidence level are labeled in each panel and help us to determine whether the
387 corresponding contribution is significant to explain the variation of simulated ozone. As
388 discussed before, EmissO₃ reflects the effects from surface emission changes on ozone
389 variations at interannual time scale. The stratospheric input reaches its seasonal
390 maximum in August, during which the stratospheric contribution is significant
391 throughout the troposphere, explaining about 66% of the simulated ozone variance at 270
392 hPa and 37% at 430 hPa. The contributions from emission changes are very small and
393 insignificant at these two levels in August. In September, the IAV of stratospheric input
394 explains about 55% of the IAV in ozone at 270 hPa. The contribution decreases but is
395 still significant at 430 hPa. The IAV of surface emissions contributes substantially to the
396 IAV of ozone in September. The influence of emissions exceeds that of the stratosphere
397 and explains about 35% of IAV in ozone at 430hPa. In December, the contribution from
398 stratospheric input to the IAV of ozone is dominant (~47%) at 270 hPa. The contribution
399 from emission is also significant at this level and explains 28% variance of IAV of ozone.
400 At 430 hPa, the contribution from emission exceeds that from stratospheric input.

401 We quantify emission contributions from three burning regions using a tagged CO
402 simulation. Figure 9 shows standardized anomalies of the tagged CO tracers over South

403 Atlantic from three burning source regions, including southern Africa (red), South
404 America (blue) and South and Southeast Asia (green) and their comparison with the
405 EmissO₃ at 270 and 430 hPa in September and December from 1992 to 2011. The direct
406 downwind transport of emissions from South America contributes most to the ozone
407 variability from emissions over this region in September at both levels and the effects are
408 most significant in the lower level (~58% at 430 hPa). In the upper troposphere, besides
409 the contribution from S. America, the uplift and cross-equator transport of pollutants
410 from South and Southeast Asia also contributes (>10%) to the ozone variation over South
411 Atlantic region. The contribution from southern Africa is small and less than 10% at both
412 levels. We also note that both StratO₃ and EmissO₃ show a minimum in 2009 and a
413 maximum in 2010. There was a strong El Niño event in the year 2009/2010. Neu et al.
414 (2014) identified the increased stratospheric circulation in 2010 driven by El
415 Niño/easterly QBO based on TES data. A few other studies (e.g., Chen et al., 2011;
416 Lewis et al., 2011) found that combined effects of 2009/2010 El Niño and warmer than
417 normal Atlantic SST produced a severe drought over S. America and caused extensive
418 biomass burning emission in 2010 dry season. Therefore, the agreements between
419 changes in the StratO₃ and EmissO₃ over 2009/2010 are at least partly driven by ENSO.
420 Similar tropospheric ozone anomalies are observed after 1997 and 2006 El Niño event.
421 Olsen et al. (2016) examined the magnitude and spatial distribution of ENSO effects on
422 tropospheric column ozone using the assimilated fields and found a statistically
423 significant negative response of tropospheric column ozone to the Niño 3.4 index over
424 South Atlantic Ocean.

425 In December, emissions from South America and southern Africa do not contribute
426 substantially to the IAV of EmissO₃. Emissions from South and Southeast Asia dominate,
427 explaining 83% and 77% variance of EmissO₃ IAV at 270 hPa and 430 hPa. The
428 pollutants from South and Southeast Asia have the stronger influence at the upper
429 troposphere because of their transport pathway as discussed in Sauvage et al. (2007).
430 Therefore, the emission contribution of tropospheric ozone IAV becomes significant at
431 270 hPa in December.

432 In summary, over the South Atlantic region, the stratospheric input plays a dominant role
433 in the upper troposphere with a seasonal maximum in August. At 430 hPa the

434 contribution from emission changes to the IAV of ozone exceeds that of stratospheric
435 input in September and December. A tagged CO simulation from 1992 to 2011 shows the
436 direct downwind transport of pollutants from South America is the largest contributor to
437 EmissO₃ in September, and it is strongest near the surface. In December, cross-equator
438 transport of South and Southeast Asia pollutants is the most important source of IAV due
439 to emissions, and the effects are stronger in the upper troposphere.

440 **3.3.2 South Indian Ocean**

441 Over the south Indian Ocean, the fitted and simulated ozone anomalies are in excellent
442 agreement (Figure 10). The explained proportion of variability in simulated ozone
443 anomalies by StratO₃ and EmissO₃ is as high as ~ 88% in August at 270 hPa. We show
444 relative contribution to the IAV in ozone due to stratospheric input and emission as
445 obtained from multiple linear regression in Figure 11. In August and September,
446 stratospheric input contributes more than 85% to ozone IAV at 270 hPa. The
447 stratospheric contribution decreases slightly but is still dominant and significant at 430
448 hPa (~49% in August and 60% in September). The emission contribution, which is
449 mainly from downwind transport of pollutants from S. America and southern Africa
450 (Figure 12), is most important at 430 hPa in September but accounts for only 13% of
451 ozone IAV. The emission contribution is smaller in August. In December, both
452 stratospheric input and surface emission influence the IAV of ozone. The contribution
453 from stratospheric input exceeds that from emissions at 270 hPa and becomes slightly
454 weaker at 430 hPa. Examining the tagged sources simulation shows that emissions from
455 South and Southeastern Asia regions are the largest source of ozone IAV at 270 hPa and
456 430 hPa in December with a stronger influence at the upper troposphere (Figure 12).

457 These results show that stratospheric ozone makes a significant contribution to the
458 tropospheric ozone variability over the South Indian Ocean, with the largest influence in
459 the upper troposphere in austral winter. Emission influence from nearby pollution in the
460 boundary layer is relatively weak and only significant in September, one month after the
461 southern hemisphere peak-burning season. In the upper troposphere, the cross-equator
462 transport of pollutants from South and Southeast Asia is the major emission source

463 affecting the ozone variability. The influence peaks in December in the upper troposphere
464 and extends to the middle troposphere.

465 **3.3.3 Tropical South Atlantic**

466 In the upper troposphere, lightning produces nitrogen oxides (NO_x) and promotes the
467 photochemical ozone production (e.g., Pickering et al., 1993). Murray et al. (2013) shows
468 that the IAV of tropical tropospheric ozone column is sensitive to the IAV of lightning
469 over the tropical south Atlantic region. We therefore add the lightning NO_x as the third
470 variable besides StratO_3 and EmissO_3 . We test whether the addition of lightning NO_x
471 improves the regression model significantly. Figure 13 shows the comparison between
472 simulated and fitted ozone anomalies without and with lightning NO_x . During the “dry
473 season” months of August and September, when the subtropical jet related STE (Karoly
474 et al., 1998; Bals-Elsholz et al., 2001; Nakamura and Shimpo, 2004) reaches a seasonal
475 maximum, the lightning activity reaches a seasonal minimum over the southern
476 hemisphere. The fitted ozone anomalies based solely on StratO_3 and EmissO_3 (red) show
477 high correlations ($r = 0.8$ in August, $r = 0.74$ in September) with that simulated from
478 GMI-CTM at 270 hPa. Agreement between simulated and fitted ozone does not change in
479 August and improves slightly in September by adding lightning NO_x in regression. In
480 September, the simulated ozone anomaly shows a minimum (~ -6 ppb) in 2007 and a
481 peak (~ 5 ppb) in 2010 at 430 hPa, but the IAV from 2007 to 2010 is almost missing in
482 the fitted ozone anomaly, which indicates that other factors drive the IAV of ozone over
483 tropical south Atlantic during this period. During the “wet season” month of December,
484 the lightning activity reaches its seasonal maximum. Our regression based on StratO_3 and
485 EmissO_3 does not capture well the IAV of GMI-CTM simulated ozone at either level.
486 The fitted ozone reproduces many of the IAV of simulated ozone after including
487 lightning NO_x in the regression, indicating a strong influence from the lightning NO_x in
488 December.

489 Figure 14 shows the regression results of relative contributions of stratospheric input and
490 surface emission on the IAV of ozone. As discussed above, the tropical south Atlantic is
491 in the descending branch of the Walker Circulation. Therefore, even though this region is
492 located in the tropics, the IAV of stratospheric input still plays a dominant role and

493 explains 60% in August and 51% in September of ozone variance in the upper
494 troposphere. The stratospheric contribution, associated with radiative descent over this
495 region, drops to less than 38% in August and 18% in September at 430 hPa but is still
496 significant during these two months. Emission influences are not significant at either
497 level in September. Examination of the simulation shows that emission contribution is
498 limited even at lower levels; the emission contribution becomes significant and explains
499 ~30% variance of ozone at ~700 hPa (not shown). In December, neither stratospheric
500 input nor emission contributes much to the IAV of ozone.

501 In the model, the lightning emissions take place in connection with deep convective
502 events (Allen et al., 2010). Increase in deep convection produces more upper tropospheric
503 NO_x from lightning, which results in more ozone production. On the other hand, deep
504 convection affects the upper tropospheric ozone budget through its direct transport of
505 surface air. In December, biomass burning in the Southern Hemisphere is at its seasonal
506 minimum. Air over tropical south Atlantic is relatively clean with low CO (Liu et al.,
507 2010). Deep convection over a clean region reduces upper tropospheric ozone by mixing
508 up ozone-poor air from near the surface. This effect could be opposite if deep convection
509 happens over a polluted region with relatively high ozone and its precursors (Lawrence et
510 al., 2003; Ziemke, et al., 2015). Use of the correlation to identify influence from the
511 lightning NO_x does not separate the two outcomes of IAV in convection, thus the sign of
512 the correlation between variations in lightning NO_x and upper tropospheric ozone can be
513 positive or negative. The correlation is positive if the contribution from lightning NO_x
514 exceeds the contribution from convective transport or if transport of polluted air increases
515 ozone. The correlation is negative if transport of clean air overwhelms ozone production
516 from lightning NO_x. Figure 15 compares the model residual after removing the
517 contributions from StratO₃ and EmissO₃ with the lightning NO_x at 270 hPa in September
518 and December. In September the IAV of lightning plays a minor but significant role in
519 the IAV of ozone in the upper troposphere. In December, the changes in lightning NO_x
520 have a significant impact on the ozone IAV, but show a negative regression ($\beta_3=-1.29$),
521 which indicates that the transport and mixing of clean surface air exceeds ozone
522 production from lightning NO_x emissions with a net negative impact of IAV in
523 convection.

524 **3.3.4 Tropical southeastern Pacific**

525 Figure 16, 17 and 18 show the similar comparisons but over the tropical southeastern
526 Pacific region. The fitted ozone anomalies show moderate but still significant correlations
527 with that simulated from GMI-CTM in August and September. In December, the fitted
528 ozone IAV agrees very well with the GMI-CTM simulated ozone IAV at 270 hPa. At 430
529 hPa the agreement collapses and the fitted ozone does not show strong IAV as seen in the
530 GMI-CTM simulated ozone (Figure 16). Figure 17 shows that IAV in stratospheric input
531 significantly affects the ozone IAV during these three months, explaining 28-40% of the
532 variance of simulated ozone at 270 hPa. Emissions contribution is quite small in August
533 and September, but is significant and explains 17% of simulated ozone IAV in December
534 at 270 hPa. The tagged CO simulations show that the tropical southeastern Pacific region
535 is influenced by nearby pollutants from South America, and also by the cross-equator
536 transport of pollutants from South and Southeast Asia (Figure 18). Previous studies (e.g.,
537 Chandra et al., 1998; Sudo and Takahashi, 2001; Chandra et al., 2002; Ziemke and
538 Chandra, 2003; Doherty et al., 2006; Chandra et al., 2009; Oman et al., 2011) show that
539 ENSO has its strongest impact in the tropical Pacific basin. In August, the ITCZ is
540 located at its northernmost location north of the Equator. Radiative sinking motion still
541 dominates over the tropical southeastern Pacific in the middle - upper troposphere (Liu et
542 al., 2010). Therefore, the emissions contribution from South America is quite small at
543 430 hPa and 270 hPa as shown in Figure 17. During an El Niño year, warmer SST with
544 increased convection and large-scale upwelling begin in August, inhibiting the radiative
545 sinking motion and resulting in ozone decrease in the middle-upper troposphere over this
546 region. Our comparison shows strong negative correlation in August between IAV of
547 middle-upper tropospheric ozone anomalies over this region and Niño 3.4 index during
548 the past twenty years (Figure 19).

549 **4 Summary and Discussion**

550 Both model simulations and GEOS-5 assimilated ozone product derived from OMI/MLS
551 show a tropospheric ozone column maximum centered over the south Atlantic from the
552 equator to 30°S. This ozone maximum extends westward to South America and the

553 eastern equatorial Pacific; it extends southeastward to southern Africa and the south
554 Indian Ocean. In this study, we use hindcast simulations from the GMI-CTM, driven by
555 assimilated MERRA meteorological fields, to interpret and quantify the relative
556 importance of the stratospheric input and surface emission to the interannual variations of
557 tropospheric ozone over four sub-regions of the SHTOM from 1992 to 2011. Over the
558 SHTOM region, IAV in the stratospheric contribution is found to be the most important
559 factor driving the IAV of ozone, especially over the upper troposphere, where O₃ changes
560 have strong radiative effects (Lacis et al., 1990). The IAV of the stratospheric
561 contribution explains a large portion of variance in the tropospheric ozone especially
562 during the austral winter season, even over two selected tropical regions. The strong
563 influence of emission on ozone IAV is largely confined to the South Atlantic region in
564 September.

565 Although the SHTOM looks like a continuous feature in the southern hemisphere, our
566 study shows that the relative importance between stratospheric input and surface
567 emissions changes over different subregions at different altitude. Over the two extra-
568 tropics regions, the IAV of stratospheric contribution explains at least 50% of variance of
569 the tropospheric ozone during its winter season. The IAV of ozone over the south Indian
570 Ocean is dominantly driven by the IAV of stratospheric ozone contribution with little or
571 no influence from surface emissions at 270 hPa and 430 hPa. Over the south Atlantic
572 region, besides the stratospheric ozone input, the IAV of surface emissions from South
573 America and southern Africa also play a big role on the IAV of ozone, especially in the
574 lower levels. The influence from emission exceeds that from the stratospheric
575 contribution on the ozone variability in September at 430 hPa. In December, the emission
576 influence mainly from remote transport of pollutants from South and Southeast Asia is
577 significant and stays high in the upper troposphere.

578 Compared to the extra-tropics regions, the influence from stratospheric input is smaller
579 but still significant in two tropical regions at both 270 hPa and 430 hPa in August and
580 September. Over tropical south Atlantic region, the IAV of stratospheric input plays a
581 dominant role and explains 60% in August and 51% in September of the ozone IAV at
582 270 hPa. The stratospheric contribution is still significant at 430 hPa, but drops to less
583 than half of that at 270 hPa. Emission contributions are not significant at these two levels,

584 even during September. Our model shows that the IAV of ozone is partially driven by the
585 IAV of lightning in September. In December, the changes in lightning NO_x have a
586 significant impact on the ozone IAV, but show a negative correlation, which indicates
587 that the transport and mixing of clean surface air exceeds ozone production from
588 lightning NO_x emissions with a net negative impact of IAV in convection. Over the
589 tropical southeastern Pacific, IAV in stratospheric input significantly affects the ozone
590 IAV during these three months, explaining 28-40% of the variance of simulated ozone at
591 270 hPa. Emissions have little or no influence in August, September at 270 hPa and 430
592 hPa, but are significant in December at 270 hPa, explaining 17% of simulated ozone
593 IAV. A further comparison of ozone and ENSO index shows that ENSO, which affects
594 the tropical convection and large-scale upwelling, shows a strong negative correlation
595 with the IAV of tropospheric ozone over this region. Therefore, the model
596 simulations/predictions with different convective parameterizations exhibit large
597 uncertainties over this region as observed in Stevenson et al. (2006) and Young et al.
598 (2013).

599 In this study, our regional analysis based on the GMI-CTM model provides valuable
600 conclusions on drivers of interannual variability over different subregions of the SHTOM
601 and how they vary with the altitude. The quantification of their relative contributions on
602 interannual time scales enhances our understanding of the IAV and, potentially, long-
603 term trends in the tropospheric ozone and furthermore their effects on the radiative
604 forcing of climate.

605 **Acknowledgement**

606 All model output used for this article can be obtained by contacting J. Liu (email:
607 junhua.liu@nasa.gov). I gratefully acknowledge the financial support by NASA's
608 Atmospheric Chemistry Modeling and Analysis Program (ACMAP) (grants
609 NNH12ZDA001N). Work was performed under contract with NASA at Goddard. I
610 would like to thank K. Pickering, L. Oman, A. Thompson, H. Liu for their helpful
611 discussion.

612 **References**

- 613 Allen, D., Pickering, K., Duncan, B., and Damon, M.: Impact of lightning NO emissions
614 on North American photochemistry as determined using the Global Modeling
615 Initiative (GMI) model, *Journal of Geophysical Research-Atmospheres*, 115,
616 10.1029/2010jd014062, 2010.
- 617 Bals-Elsholz, T. M., Atallah, E. H., Bosart, L. F., Wasula, T. A., Cempa, M. J., and Lupo,
618 A. R.: The wintertime Southern Hemisphere split jet: Structure, variability, and
619 evolution, *Journal of Climate*, 14, 4191-4215, 10.1175/1520-
620 0442(2001)014<4191:twshsj>2.0.co;2, 2001.
- 621 Bjercknes, J.: Atmospheric teleconnections from the equatorial Pacific, *Mon. Weather*
622 *Rev.*, 97(3), 163–172, 1969.
- 623 Chandra, S., Ziemke, J. R., Min, W., and Read, W. G.: Effects of 1997-1998 El Nino on
624 tropospheric ozone and water vapor, *Geophysical Research Letters*, 25, 3867-
625 3870, 10.1029/98gl02695, 1998.
- 626 Chandra, S., Ziemke, J. R., Bhartia, P. K., and Martin, R. V.: Tropical tropospheric
627 ozone: Implications for dynamics and biomass burning, *Journal of Geophysical*
628 *Research-Atmospheres*, 107, 10.1029/2001jd000447, 2002.
- 629 Chandra, S., Ziemke, J. R., Duncan, B. N., Diehl, T. L., Livesey, N. J., and Froidevaux,
630 L.: Effects of the 2006 El Nino on tropospheric ozone and carbon monoxide:
631 implications for dynamics and biomass burning, *Atmospheric Chemistry and*
632 *Physics*, 9, 4239-4249, 2009.
- 633 Chen, Y., Randerson, J. T., Morton, D. C., DeFries, R. S., Collatz, G. J., Kasibhatla, P.
634 S., Giglio, L., Jin, Y., and Marlier, M. E.: Forecasting Fire Season Severity in
635 South America Using Sea Surface Temperature Anomalies, *Science*, 334, 787-
636 791, 10.1126/science.1209472, 2011.
- 637 Chevan, A., and Sutherland, M.: HIERARCHICAL PARTITIONING, *American*
638 *Statistician*, 45, 90-96, 10.2307/2684366, 1991.
- 639 Chin, M., Ginoux, P., Kinne, S., Torres, O., Holben, B. N., Duncan, B. N., Martin, R. V.,
640 Logan, J. A., Higurashi, A., and Nakajima, T.: Tropospheric aerosol optical
641 thickness from the GOCART model and comparisons with satellite and Sun
642 photometer measurements, *J ATMOS SCI*, 59, 461-483, 2002.
- 643 Danielsen, E. F.: Stratospheric-Tropospheric Exchange Based on Radioactivity, Ozone
644 and Potential Vorticity Stratospheric-Tropospheric Exchange Based on
645 Radioactivity, Ozone and Potential Vorticity, *Journal of the Atmospheric*
646 *Sciences*, 25, 502-518, 10.1175/1520-0469(1968).
- 647 Doherty, R. M., Stevenson, D. S., Johnson, C. E., Collins, W. J., and Sanderson, M. G.:
648 Tropospheric ozone and El Nino-Southern Oscillation: Influence of atmospheric
649 dynamics, biomass burning emissions, and future climate change, *Journal of*
650 *Geophysical Research-Atmospheres*, 111, 10.1029/2005jd006849, 2006.
- 651 Duncan, B. N., Martin, R. V., Staudt, A. C., Yevich, R., and Logan, J. A.: Interannual and
652 seasonal variability of biomass burning emissions constrained by satellite
653 observations, *Journal of Geophysical Research-Atmospheres*, 108,
654 10.1029/2002jd002378, 2003.

655 Duncan, B. N., Strahan, S. E., Yoshida, Y., Steenrod, S. D., and Livesey, N.: Model study
656 of the cross-tropopause transport of biomass burning pollution, *ATMOS CHEM*
657 *PHYS*, 7, 3713-3736, 2007.

658 Eyring, V., Lamarque, J.-F., Hess, P., Arfeuille, F., Bowman, K., Chipperfield, M. P.,
659 Duncan, B., Fiore, A., Gettelman, A., Giorgetta, M. A., Granier, C., Kinnison, M.
660 H. D., Kunze, M., Langematz, U., Luo, B., Martin, R., Matthes, K., Newman, P.
661 A., Peter, T., Robock, A., Ryerson, T., Saiz-Lopez, A., Salawitch, R., Schultz, M.,
662 Shepherd, T. G., Shindell, D., Staehelin, J., Tegtmeier, S., Thomason, L., Tilmes,
663 S., Vernier, J.-P., Waugh, D. W., and Young, P. J.: Overview of IGAC/SPARC
664 Chemistry-Climate Model Initiative (CCMI) Community Simulations in
665 Support of Upcoming Ozone and Climate Assessments. In: *SPARC*
666 *Newsletter* 40, 48, WMO/SPARC, Zürich, 2013.

667 Fishman, J., Watson, C. E., Larsen, J. C., and Logan, J. A.: DISTRIBUTION OF
668 TROPOSPHERIC OZONE DETERMINED FROM SATELLITE DATA, *Journal*
669 *of Geophysical Research-Atmospheres*, 95, 3599-3617,
670 10.1029/JD095iD04p03599, 1990.

671 Folkins, I., Braun, C., Thompson, A. M., and Witte, J.: Tropical ozone as an indicator of
672 deep convection, *Journal of Geophysical Research-Atmospheres*, 107,
673 10.1029/2001jd001178, 2002.

674 Groemping, U.: Two simple estimators of relative importance in linear regression based
675 on variance decomposition - Response, *American Statistician*, 61, 282-283, 2007.

676 Guenther, A., Karl, T., Harley, P., Wiedinmyer, C., Palmer, P. I., and Geron, C.:
677 Estimates of global terrestrial isoprene emissions using MEGAN (Model of
678 Emissions of Gases and Aerosols from Nature), *ATMOS CHEM PHYS*, 6, 3181-
679 3210, 2006.

680 Hess, P., and Mahowald, N.: Interannual variability in hindcasts of atmospheric
681 chemistry: the role of meteorology, *ATMOS CHEM PHYS*, 9, 5261-5280,
682 10.5194/acp-9-5261-2009, 2009.

683 Hoskins, B. J., and Rodwell, M. J.: A MODEL OF THE ASIAN SUMMER MONSOON
684 .1. THE GLOBAL-SCALE, *Journal of the Atmospheric Sciences*, 52, 1329-1340,
685 10.1175/1520-0469(1995)052<1329:amotas>2.0.co;2, 1995.

686 Jacob, D. J., Heikes, B. G., Fan, S. M., Logan, J. A., Mauzerall, D. L., Bradshaw, J. D.,
687 Singh, H. B., Gregory, G. L., Talbot, R. W., Blake, D. R., and Sachse, G. W.:
688 Origin of ozone and NO_x in the tropical troposphere: A photochemical analysis of
689 aircraft observations over the South Atlantic basin, *Journal of Geophysical*
690 *Research-Atmospheres*, 101, 24235-24250, 10.1029/96jd00336, 1996.

691 Jenkins, G. S., and Ryu, J. H.: Space-borne observations link the tropical atlantic ozone
692 maximum and paradox to lightning, *Atmospheric Chemistry and Physics*, 4, 361-
693 375, 2004a.

694 Jenkins, G. S., and Ryu, J. H.: Linking horizontal and vertical transports of biomass fire
695 emissions to the tropical Atlantic ozone paradox during the Northern Hemisphere
696 winter season: climatology, *Atmospheric Chemistry and Physics*, 4, 449-469,
697 2004b.

698 Jourdain, L., Worden, H. M., Worden, J. R., Bowman, K., Li, Q., Eldering, A., Kulawik,
699 S. S., Osterman, G., Boersma, K. F., Fisher, B., Rinsland, C. P., Beer, R., and
700 Gunson, M.: Tropospheric vertical distribution of tropical Atlantic ozone

701 observed by TES during the northern African biomass burning season,
702 Geophysical Research Letters, 34, 10.1029/2006gl028284, 2007.

703 Julian, P. R., and Chervin, R. M.: A study of the Southern Oscillation and Walker
704 Circulation phenomenon, *Mon. Weather Rev.*, 106(10), 1433–1451, 1978.

705 Karoly, D. J., Vincent, D. G., and Schrage, J. M.: *Meteorology of the Southern*
706 *Hemisphere, General circulation*, American Meteorological Society, 45 Beacon
707 St., Boston, MA, 02108, 1998.

708 Kim, P. S., Jacob, D. J., Liu, X., Warner, J. X., Yang, K., Chance, K., Thouret, V., and
709 Nedelec, P.: Global ozone-CO correlations from OMI and AIRS: constraints on
710 tropospheric ozone sources, *Atmospheric Chemistry and Physics*, 13, 9321-9335,
711 10.5194/acp-13-9321-2013, 2013.

712 Kruskal, W.: RELATIVE IMPORTANCE BY AVERAGING OVER ORDERINGS,
713 *American Statistician*, 41, 6-10, 10.2307/2684310, 1987.

714 Lacis, A. A., Wuebbles, D. J., and Logan, J. A.: RADIATIVE FORCING OF CLIMATE
715 BY CHANGES IN THE VERTICAL-DISTRIBUTION OF OZONE, *Journal of*
716 *Geophysical Research-Atmospheres*, 95, 9971-9981, 10.1029/JD095iD07p09971,
717 1990.

718 Lawrence, M. G., von Kuhlmann, R., Salzmann, M., and Rasch, P. J.: The balance of
719 effects of deep convective mixing on tropospheric ozone, *Geophysical Research*
720 *Letters*, 30, 10.1029/2003gl017644, 2003.

721 Lewis, S. L., Brando, P. M., Phillips, O. L., van der Heijden, G. M. F., and Nepstad, D.:
722 The 2010 Amazon Drought, *Science*, 331, 554-554, 10.1126/science.1200807,
723 2011.

724 Lin, M., Fiore, A. M., Cooper, O. R., Horowitz, L. W., Langford, A. O., Levy II, H.,
725 Johnson, B. J., Vaishali Naik, V., Oltmans, S. J., and Senff, C. J.: Springtime high
726 surface ozone events over the western United States: Quantifying the role of
727 stratospheric intrusions, Submitted to *JGR-Atmosphere*, CalNex Special Section,
728 2012.

729 Liu, J., Logan, J. A., Jones, D. B. A., Livesey, N. J., Megretskaia, I., Carouge, C., and
730 Nedelec, P.: Analysis of CO in the tropical troposphere using Aura satellite data
731 and the GEOS-Chem model: insights into transport characteristics of the GEOS
732 meteorological products, *Atmospheric Chemistry and Physics*, 10, 12207-12232,
733 10.5194/acp-10-12207-2010, 2010.

734 Liu, J., Logan, J. A., Murray, L. T., Pumphrey, H. C., Schwartz, M. J., and Megretskaia,
735 I. A.: Transport analysis and source attribution of seasonal and interannual
736 variability of CO in the tropical upper troposphere and lower stratosphere,
737 *Atmospheric Chemistry and Physics*, 13, 129-146, 10.5194/acp-13-129-2013,
738 2013.

739 Liu, J., Rodriguez, J. M., Thompson, A. M., Logan, J. A., Douglass, A. R., Olsen, M. A.,
740 Steenrod, S. D., and Posny, F.: Origins of tropospheric ozone interannual
741 variation over Reunion: A model investigation, *Journal of Geophysical Research-*
742 *Atmospheres*, 121, 521-537, 10.1002/2015jd023981, 2016.

743 Logan, J. A., Prather, M. J., Wofsy, S. C., and McElroy, M. B.: TROPOSPHERIC
744 CHEMISTRY - A GLOBAL PERSPECTIVE, *Journal of Geophysical Research-*
745 *Oceans and Atmospheres*, 86, 7210-7254, 10.1029/JC086iC08p07210, 1981.

746 Logan, J. A., Megretskaya, I., Nassar, R., Murray, L. T., Zhang, L., Bowman, K. W.,
 747 Worden, H. M., and Luo, M.: Effects of the 2006 El Niño on tropospheric
 748 composition as revealed by data from the Tropospheric Emission Spectrometer
 749 (TES), *Geophysical Research Letters*, 35, 10.1029/2007gl031698, 2008.

750 Martin, R. V., Jacob, D. J., Logan, J. A., Bey, I., Yantosca, R. M., Staudt, A. C., Li, Q.
 751 B., Fiore, A. M., Duncan, B. N., Liu, H. Y., Ginoux, P., and Thouret, V.:
 752 Interpretation of TOMS observations of tropical tropospheric ozone with a global
 753 model and in situ observations, *Journal of Geophysical Research-Atmospheres*,
 754 107, 10.1029/2001jd001480, 2002.

755 Murray, L. T., Logan, J. A., and Jacob, D. J.: Interannual variability in tropical
 756 tropospheric ozone and OH: The role of lightning, *Journal of Geophysical
 757 Research-Atmospheres*, 118, 11468-11480, 10.1002/jgrd.50857, 2013.

758 Nakamura, H., and Shimpo, A.: Seasonal Variations in the Southern Hemisphere Storm
 759 Tracks and Jet Streams as Revealed in a Reanalysis Dataset., *J. Climate*, 17,
 760 1828–1844., 2004.

761 Neu, J. L., Flury, T., Manney, G. L., Santee, M. L., Livesey, N. J., and Worden, J.:
 762 Tropospheric ozone variations governed by changes in stratospheric circulation,
 763 *Nature Geoscience*, 7, 340-344, 10.1038/ngeo2138, 2014.

764 Olivier, J. G. J., Van Aardenne, J. A., Dentener, F. J., Pagliari, V., Ganzeveld, L. N., and
 765 Peters, J. A. H. W.: Recent trends in global greenhouse gas emissions: regional
 766 trends and spatial distribution of key sources, in: *Non-CO2 Greenhouse Gases
 767 (NCGG-4)*, coordinator: van Amstel, A., Millpress, Rotterdam, ISBN 905966
 768 043 9, 325–330., 2005.

769 Olsen, M. A., Wargan, K., and Pawson, S.: Tropospheric column ozone response to
 770 ENSO in GEOS-5 assimilation of OMI and MLS ozone data, *Atmospheric
 771 Chemistry and Physics*, 16, 7091-7103, 10.5194/acp-16-7091-2016, 2016.

772 Oman, L. D., Ziemke, J. R., Douglass, A. R., Waugh, D. W., Lang, C., Rodriguez, J. M.,
 773 and Nielsen, J. E.: The response of tropical tropospheric ozone to ENSO,
 774 *Geophysical Research Letters*, 38, 10.1029/2011gl047865, 2011.

775 Oman, L. D., Douglass, A. R., Ziemke, J. R., Rodriguez, J. M., Waugh, D. W., and
 776 Nielsen, J. E.: The ozone response to ENSO in Aura satellite measurements and a
 777 chemistry-climate simulation, *Journal of Geophysical Research-Atmospheres*,
 778 118, 965-976, 10.1029/2012jd018546, 2013.

779 Pickering, K. E., Thompson, A. M., Tao, W. K., and Kucsera, T. L.: UPPER
 780 TROPOSPHERIC OZONE PRODUCTION FOLLOWING MESOSCALE
 781 CONVECTION DURING STEP EMEX, *Journal of Geophysical Research-
 782 Atmospheres*, 98, 8737-8749, 10.1029/93jd00875, 1993.

783 Pickering, K. E., Thompson, A. M., Wang, Y. S., Tao, W. K., McNamara, D. P.,
 784 Kirchhoff, V., Heikes, B. G., Sachse, G. W., Bradshaw, J. D., Gregory, G. L., and
 785 Blake, D. R.: Convective transport of biomass burning emissions over Brazil
 786 during TRACE A, *Journal of Geophysical Research-Atmospheres*, 101, 23993-
 787 24012, 10.1029/96jd00346, 1996.

788 Prather, M. J., Zhu, X., Tang, Q., Hsu, J. N., and Neu, J. L.: An atmospheric chemist in
 789 search of the tropopause, *J GEOPHYS RES-ATMOS*, 116, D04306,
 790 10.1029/2010jd014939, 2011.

791 Rienecker, M. M., Suarez, M. J., Gelaro, R., Todling, R., Bacmeister, J., Liu, E.,
792 Bosilovich, M. G., Schubert, S. D., Takacs, L., Kim, G.-K., Bloom, S., Chen, J.,
793 Collins, D., Conaty, A., Da Silva, A., Gu, W., Joiner, J., Koster, R. D., Lucchesi,
794 R., Molod, A., Owens, T., Pawson, S., Pegion, P., Redder, C. R., Reichle, R.,
795 Robertson, F. R., Ruddick, A. G., Sienkiewicz, M., and Woollen, J.: MERRA:
796 NASA's Modern-Era Retrospective Analysis for Research and Applications,
797 *Journal of Climate*, 24, 3624-3648, 10.1175/jcli-d-11-00015.1, 2011.

798 Rodwell, M. J., and Hoskins, B. J.: Subtropical anticyclones and summer monsoons,
799 *Journal of Climate*, 14, 3192-3211, 10.1175/1520-
800 0442(2001)014<3192:saasm>2.0.co;2, 2001.

801 Sauvage, B., Thouret, V., Thompson, A. M., Witte, J. C., Cammas, J. P., Nedelec, P., and
802 Athier, G.: Enhanced view of the "tropical Atlantic ozone paradox" and "zonal
803 wave one" from the in situ MOZAIC and SHADOZ data, *Journal of Geophysical
804 Research-Atmospheres*, 111, 10.1029/2005jd006241, 2006.

805 Sauvage, B., Martin, R. V., van Donkelaar, A., and Ziemke, J. R.: Quantification of the
806 factors controlling tropical tropospheric ozone and the South Atlantic maximum,
807 *Journal of Geophysical Research-Atmospheres*, 112, 10.1029/2006jd008008,
808 2007.

809 Solomon, S., Thompson, D. W. J., Portmann, R. W., Oltmans, S. J., and Thompson, A.
810 M.: On the distribution and variability of ozone in the tropical upper troposphere:
811 Implications for tropical deep convection and chemical-dynamical coupling,
812 *Geophysical Research Letters*, 32, 10.1029/2005gl024323, 2005.

813 Stevenson, D. S., Dentener, F. J., Schultz, M. G., Ellingsen, K., van Noije, T. P. C., Wild,
814 O., Zeng, G., Amann, M., Atherton, C. S., Bell, N., Bergmann, D. J., Bey, I.,
815 Butler, T., Cofala, J., Collins, W. J., Derwent, R. G., Doherty, R. M., Drevet, J.,
816 Eskes, H. J., Fiore, A. M., Gauss, M., Hauglustaine, D. A., Horowitz, L. W.,
817 Isaksen, I. S. A., Krol, M. C., Lamarque, J. F., Lawrence, M. G., Montanaro, V.,
818 Muller, J. F., Pitari, G., Prather, M. J., Pyle, J. A., Rast, S., Rodriguez, J. M.,
819 Sanderson, M. G., Savage, N. H., Shindell, D. T., Strahan, S. E., Sudo, K., and
820 Szopa, S.: Multimodel ensemble simulations of present-day and near-future
821 tropospheric ozone, *Journal of Geophysical Research-Atmospheres*, 111,
822 10.1029/2005jd006338, 2006.

823 Stohl, A., Bonasoni, P., Cristofanelli, P., Collins, W., Feichter, J., Frank, A., Forster, C.,
824 Gerasopoulos, E., Gaggeler, H., James, P., Kentarchos, T., Kromp-Kolb, H.,
825 Kruger, B., Land, C., Meloan, J., Papayannis, A., Priller, A., Seibert, P., Sprenger,
826 M., Roelofs, G. J., Scheel, H. E., Schnabel, C., Siegmund, P., Tobler, L., Trickl,
827 T., Wernli, H., Wirth, V., Zanis, P., and Zerefos, C.: Stratosphere-troposphere
828 exchange: A review, and what we have learned from STACCATO, *Journal of
829 Geophysical Research-Atmospheres*, 108, 10.1029/2002jd002490, 2003.

830 Strahan, S. E., Duncan, B. N., and Hoor, P.: Observationally derived transport diagnostics
831 for the lowermost stratosphere and their application to the GMI chemistry and
832 transport model, *ATMOS CHEM PHYS*, 7, 2435-2445, 2007.

833 Strahan, S. E., Douglass, A. R., and Newman, P. A.: The contributions of chemistry and
834 transport to low arctic ozone in March 2011 derived from Aura MLS
835 observations, *Journal of Geophysical Research-Atmospheres*, 118, 1563-1576,
836 10.1002/jgrd.50181, 2013.

837 Strode, S. A., Rodriguez, J. M., Logan, J. A., Cooper, O. R., Witte, J. C., Lamsal, L. N.,
838 Damon, M., Van Aartsen, B., Steenrod, S. D., and Strahan, S. E.: Trends and
839 variability in surface ozone over the United States, *Journal of Geophysical*
840 *Research-Atmospheres*, 120, 9020-9042, 10.1002/2014jd022784, 2015.

841 Sudo, K., and Takahashi, M.: Simulation of tropospheric ozone changes during 1997-
842 1998 El Nino: Meteorological impact on tropospheric photochemistry,
843 *Geophysical Research Letters*, 28, 4091-4094, 10.1029/2001gl013335, 2001.

844 Thompson, A. M., Pickering, K. E., McNamara, D. P., Schoeberl, M. R., Hudson, R. D.,
845 Kim, J. H., Browell, E. V., Kirchhoff, V., and Nganga, D.: Where did
846 tropospheric ozone over southern Africa and the tropical Atlantic come from in
847 October 1992? Insights from TOMS, GTE TRACE A, and SAFARI 1992, *Journal*
848 *of Geophysical Research-Atmospheres*, 101, 24251-24278, 10.1029/96jd01463,
849 1996.

850 Thompson, A. M., Witte, J. C., McPeters, R. D., Oltmans, S. J., Schmidlin, F. J., Logan,
851 J. A., Fujiwara, M., Kirchhoff, V., Posny, F., Coetzee, G. J. R., Hoegger, B.,
852 Kawakami, S., Ogawa, T., Johnson, B. J., Vomel, H., and Labow, G.: Southern
853 Hemisphere Additional Ozonesondes (SHADOZ) 1998-2000 tropical ozone
854 climatology - 1. Comparison with Total Ozone Mapping Spectrometer (TOMS)
855 and ground-based measurements, *Journal of Geophysical Research-Atmospheres*,
856 108, 10.1029/2001jd000967, 2003.

857 Thouret, V., Saunois, M., Minga, A., Mariscal, A., Sauvage, B., Solete, A., Agbangla, D.,
858 Nedelec, P., Mari, C., Reeves, C. E., and Schlager, H.: An overview of two years
859 of ozone radio soundings over Cotonou as part of AMMA, *Atmospheric*
860 *Chemistry and Physics*, 9, 6157-6174, 2009.

861 Tocquer, F., Barret, B., Mari, C., Le Flochmoen, E., Cammas, J. P., and Sauvage, B.: An
862 upper tropospheric 'ozone river' from Africa to India during the 2008 Asian post-
863 monsoon season, *Tellus Series B-Chemical and Physical Meteorology*, 67,
864 10.3402/tellusb.v67.25350, 2015.

865 van der Werf, G. R., Randerson, J. T., Giglio, L., Collatz, G. L., Mu, M., Kasibhatla, P.
866 S., Morton, D. C., DeFries, R. S., Jin, Y., and T.T., v. L.: Global fire emissions
867 and the contribution of deforestation, savanna, forest, agricultural, and peat fires
868 (1997-2009), *ATMOS CHEM PHYS*, 10, 16153-16230, 2010.

869 Voulgarakis, A., Savage, N. H., Wild, O., Braesicke, P., Young, P. J., Carver, G. D., and
870 Pyle, J. A.: Interannual variability of tropospheric composition: the influence of
871 changes in emissions, meteorology and clouds, *Atmospheric Chemistry and*
872 *Physics*, 10, 2491-2506, 10.5194/acp-10-2491-2010, 2010.

873 Voulgarakis, A., Hadjinicolaou, P., and Pyle, J. A.: Increases in global tropospheric
874 ozone following an El Nino event: examining stratospheric ozone variability as a
875 potential driver, *Atmospheric Science Letters*, 12, 228-232, 10.1002/asl.318,
876 2011.

877 Voulgarakis, A., Marlier, M. E., Faluvegi, G., Shindell, D. T., Tsigaridis, K., and
878 Mangeon, S.: Interannual variability of tropospheric trace gases and aerosols: The
879 role of biomass burning emissions, *Journal of Geophysical Research-*
880 *Atmospheres*, 120, 7157-7173, 10.1002/2014jd022926, 2015.

881 Wargan, K., Pawson, S., Olsen, M. A., Witte, J. C., Douglass, A. R., Ziemke, J. R.,
882 Strahan, S. E., and Nielsen, J. E.: The global structure of upper troposphere-lower

883 stratosphere ozone in GEOS-5: A multiyear assimilation of EOS Aura data,
884 Journal of Geophysical Research-Atmospheres, 120, 2013-2036,
885 10.1002/2014jd022493, 2015.

886 Weller, R., Lilischkis, R., Schrems, O., Neuber, R., and Wessel, S.: Vertical ozone
887 distribution in the marine atmosphere over the central Atlantic Ocean (56 degrees
888 S 50 degrees N), Journal of Geophysical Research-Atmospheres, 101, 1387-1399,
889 10.1029/95jd02838, 1996.

890 WMO: Scientific Assessment of Ozone Depletion: 2014, Global Ozone Research and
891 Monitoring Project, World Meteorological Organization, Geneva, Switzerland,
892 2014.

893 Zeng, G., and Pyle, J. A.: Influence of El Nino Southern Oscillation on
894 stratosphere/troposphere exchange and the global tropospheric ozone budget,
895 Geophysical Research Letters, 32, 10.1029/2004gl021353, 2005.

896 Ziemke, J. R., Chandra, S., Thompson, A. M., and McNamara, D. P.: Zonal asymmetries
897 in southern hemisphere column ozone: Implications of biomass burning, Journal
898 of Geophysical Research-Atmospheres, 101, 14421-14427, 10.1029/96jd01057,
899 1996.

900 Ziemke, J. R., and Chandra, S.: La Nina and El Nino-induced variabilities of ozone in the
901 tropical lower atmosphere during 1970-2001, Geophysical Research Letters, 30,
902 10.1029/2002gl016387, 2003.

903 Ziemke, J. R., Chandra, S., Oman, L. D., and Bhartia, P. K.: A new ENSO index derived
904 from satellite measurements of column ozone, Atmospheric Chemistry and
905 Physics, 10, 3711-3721, 2010.

906 Ziemke, J. R., Olsen, M. A., Witte, J. C., Douglass, A. R., Strahan, S. E., Wargan, K.,
907 Liu, X., Schoeberl, M. R., Yang, K., Kaplan, T. B., Pawson, S., Duncan, B. N.,
908 Newman, P. A., Bhartia, P. K., and Heney, M. K.: Assessment and applications of
909 NASA ozone data products derived from Aura OMI/MLS satellite measurements
910 in context of the GMI chemical transport model, Journal of Geophysical
911 Research-Atmospheres, 119, 5671-5699, 10.1002/2013jd020914, 2014.

912 Ziemke, J.R., A.R. Douglass, L.D. Oman, S.E. Strahan, and B.N. Duncan, "Tropospheric
913 ozone variability in the tropics from ENSO to MJO and shorter timescales",
914 Atmos. Chem. Phys. Discuss., 15, 6373-6401, doi:10.5194/acpd-15-6373-2015,
915 2015.

916

917

918

919

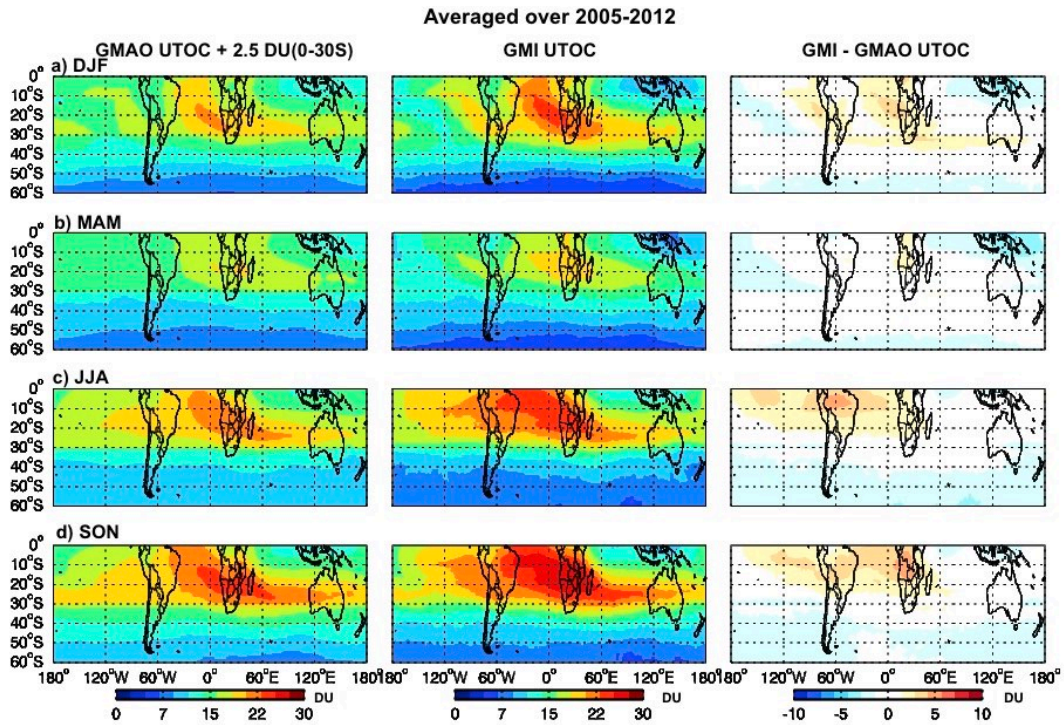
920

921

922

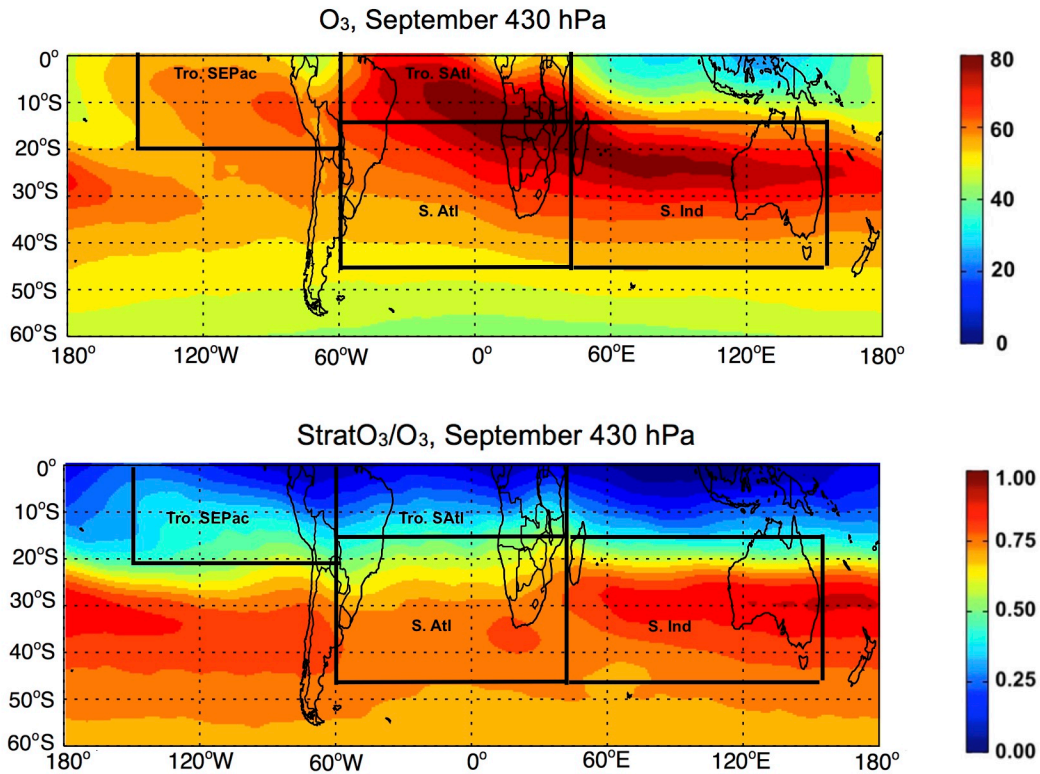
923

924 **Figures:**

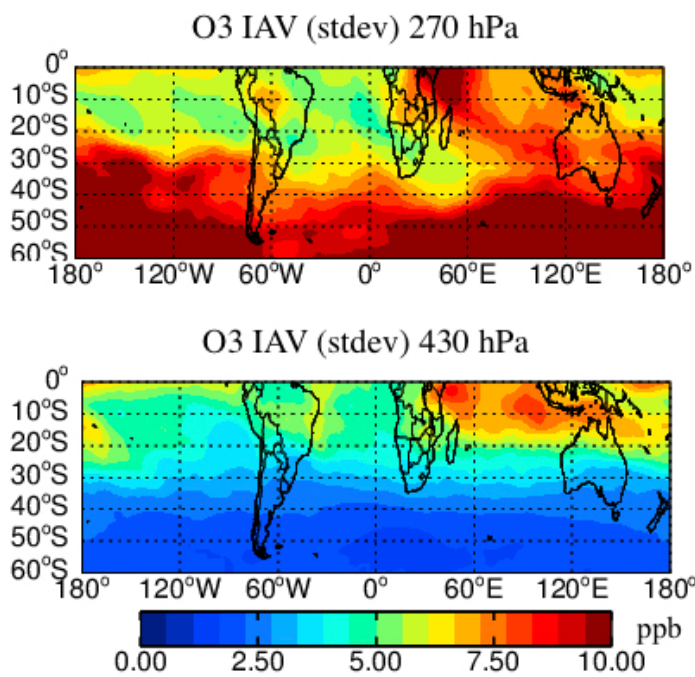


925

926 **Figure 1:** Seasonal climatology of upper tropospheric column ozone (UTOC, integrated from 500 hPa to the
927 tropopause) (in Dobson Units) for (a) December-January-February (DJF), (b) March-April-May (MAM), (c)
928 June-July-August (JJA), and (d) September-October-November (SON) averaged from 2005 to 2012 for GMAO
929 assimilated ozone (left) and GMI-CTM Hindcast-VE ozone (middle) and their absolute difference (right). The
930 GMAO assimilated ozone has been adjusted by adding 2.5 DU in 0-30° S based on Wargan et al. (2015).



931
 932 **Figure 2: The simulated ozone (top) and the $\text{StratO}_3/\text{O}_3$ (bottom) at 430 hPa averaged over 1992-2011 in**
 933 **September. Stronger stratospheric influence happens over southern hemisphere centered on 30° S, co-locating**
 934 **with subtropical jet stream regions with descending stratospheric air. The black boxes show four regions**
 935 **discussed in this study. From left to right: (1) Tropical southeastern Pacific (0-20° S, 150° W-60° W); (2)**
 936 **Tropical South Atlantic region (0-15° S, 60° W-40° E); (3) Subtropical South Atlantic region (15° S-45° S, 60° W-**
 937 **40° E); (4) Subtropical South Indian Ocean (15° S-45° S, 40° E-150° E).**



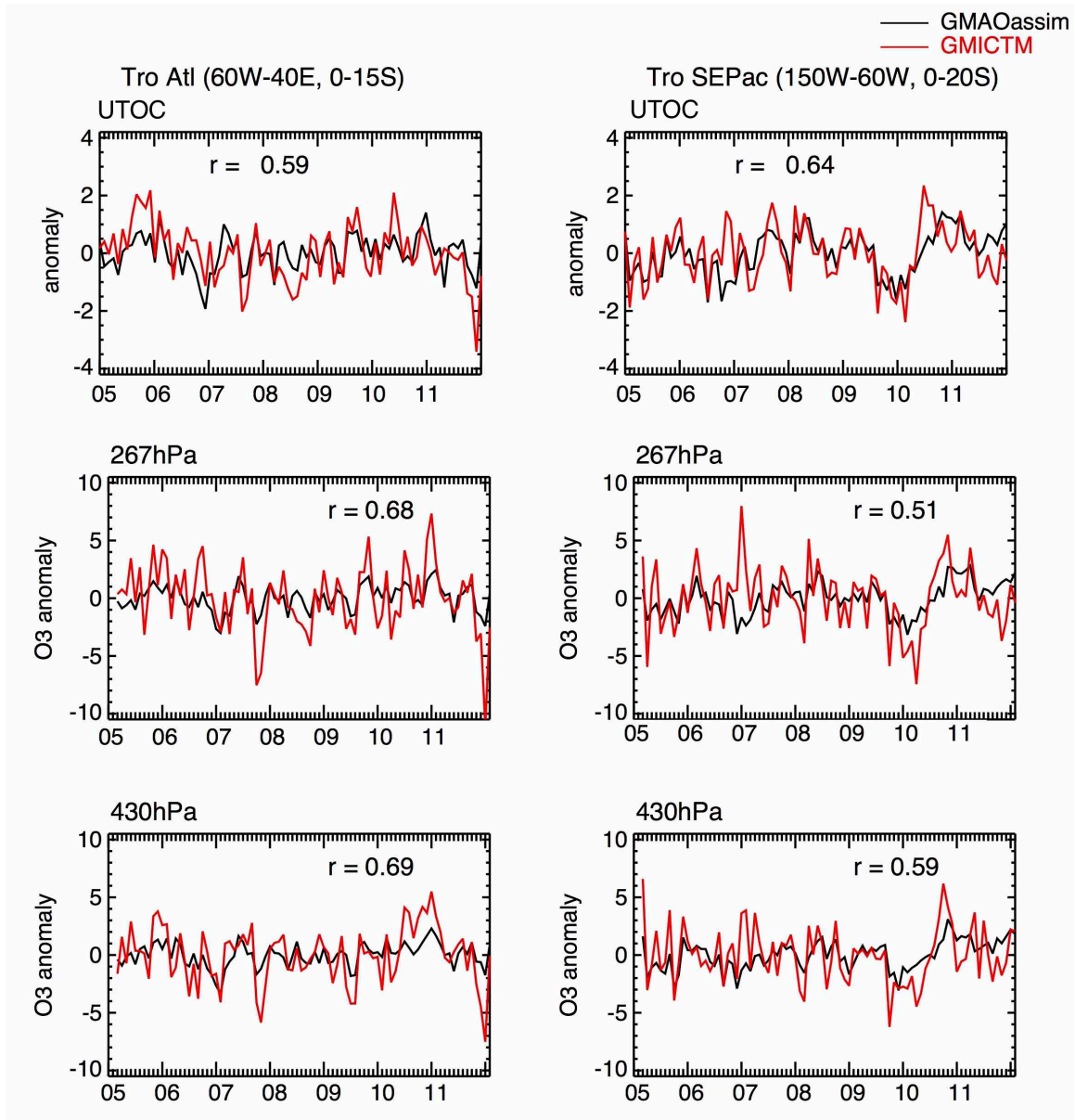
938

939

Figure 3: The interannual variations (IAV, unit of ppb) of simulated ozone at 270 hPa (top) and 430 hPa (bottom). The standard deviation of ozone anomalies (removing the monthly mean) over 1991-2011 represents the IAV.

941

942

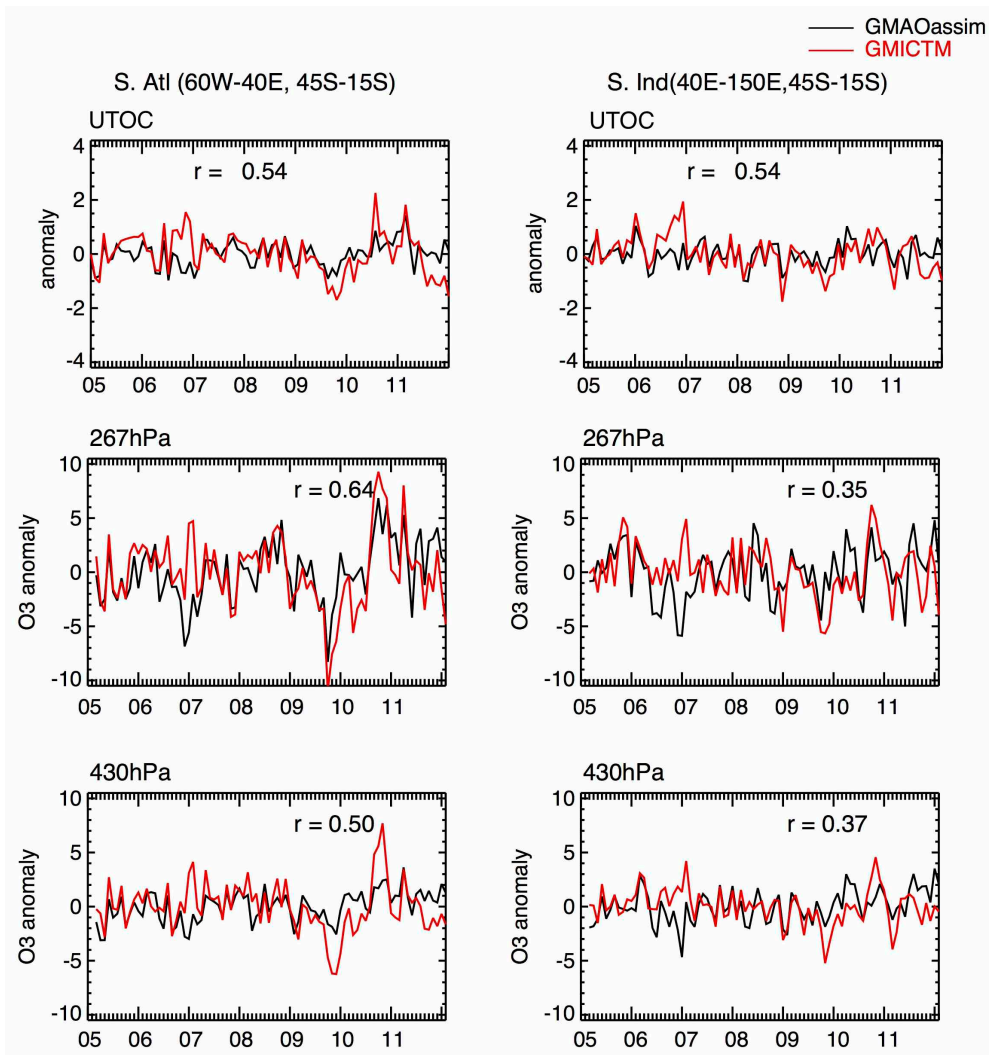


943

944

Figure 4: Time series plots of upper tropospheric ozone column (UTOC, integrated from 500 hPa to the tropopause; unit: DU) anomalies and tropospheric ozone anomalies (unit: ppb) at 270 hPa and 430 hPa from GMAO assimilated data (black) and GMI-CTM (red) over (left) Tropical South Atlantic region (0-15° S, 60° W-40° E); (right) Tropical southeastern Pacific (0-20° S, 150° W-60° W) from 2005 to 2011. The anomalies are calculated by removing the monthly mean averaged from 2005 to 2011.

948



949

950

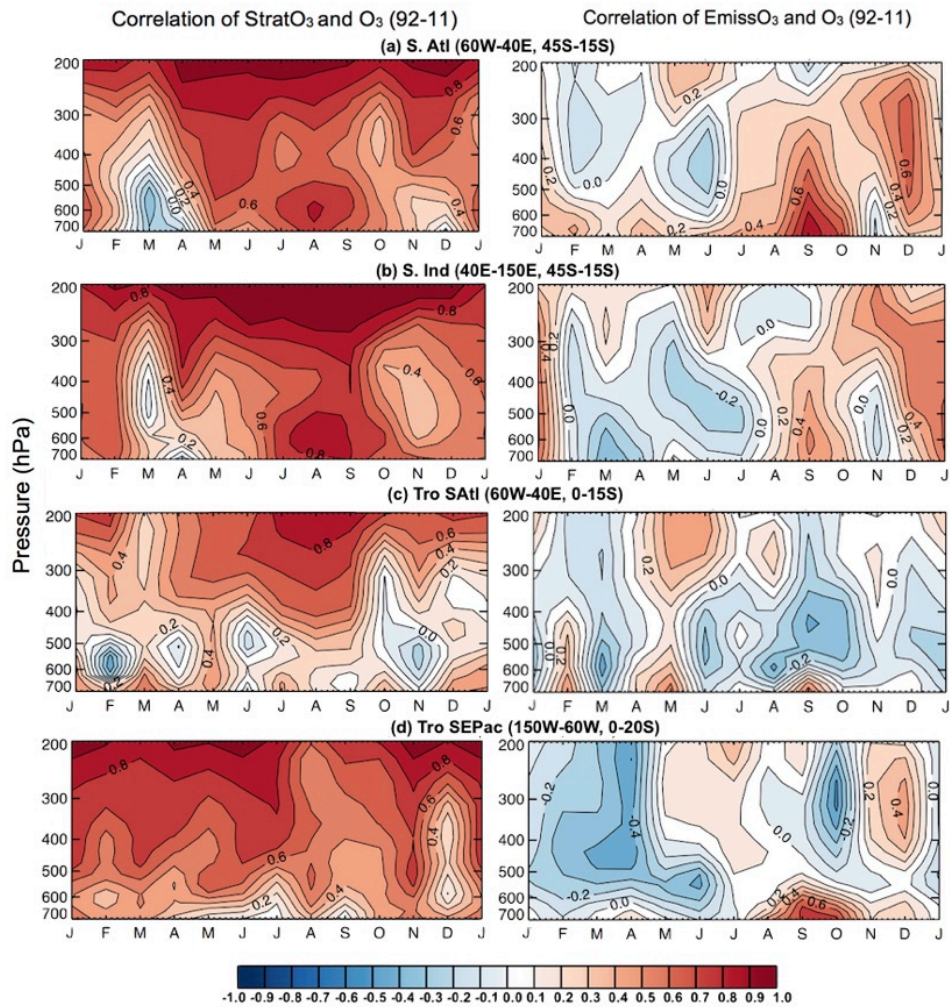
951

952

953

954

Figure 5: Time series plots of upper tropospheric ozone column (UTOC, integrated from 500 hPa to the tropopause; unit: DU) anomalies and tropospheric ozone anomalies (unit: ppb) at 270 hPa and 430 hPa from GMAO assimilated data (black) and GMI-CTM (red) over (left) South Atlantic (15° S-45° S, 60° W-40° E); (right) South Indian Ocean (15° S-45° S, 40° E-150° E) from 2005 to 2011. The anomalies are calculated by removing the monthly mean averaged from 2005 to 2011.



955

956

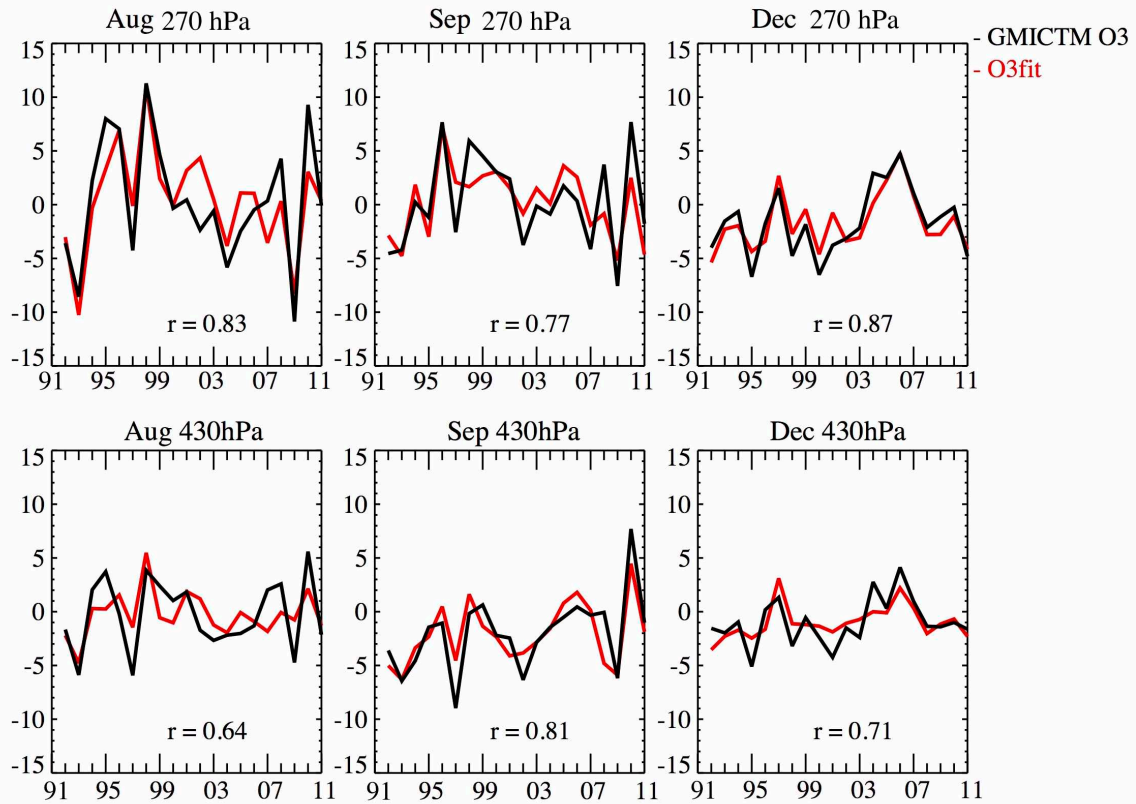
957

958

959

Figure 6: Monthly profile maps of correlations coefficients between ozone and left) StratO₃, right) EmissO₃ from 1992 to 2011 over (a) South Atlantic (15° S-45° S, 60° W-40° E); (b) South Indian Ocean (15° S-45° S, 40° E-150° E); (c) Tropical South Atlantic region (0-15° S, 60° W-40° E); (d) Tropical southeastern Pacific (0-20° S, 150° W-60° W). Y-axis is pressure in unit hPa.

S. Atl (60W-40E, 45S-15S)



960

961

962

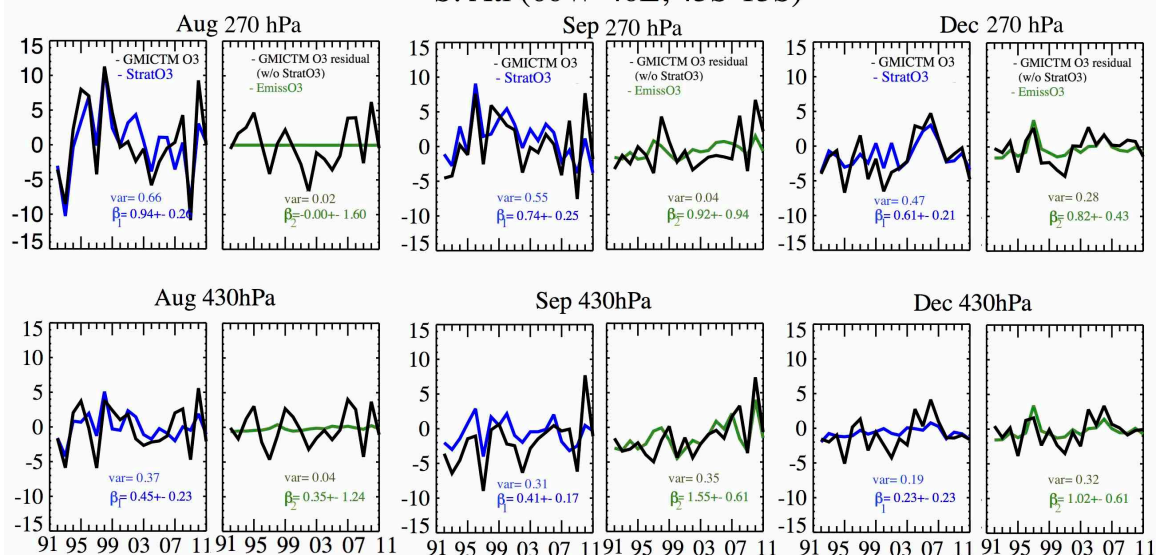
963

964

965

Figure 7: Comparison of the simulated ozone anomalies and the calculated ozone anomalies relying on two predictor variables: StratO₃, EmissO₃ at 270 hPa and 430 hPa over South Atlantic region. Three panels show results from August (left), September (middle) and December (right) from 1992 to 2011. Unit for y-axis is ppb.

S. Atl (60W-40E, 45S-15S)



966

967

968

969

970

971

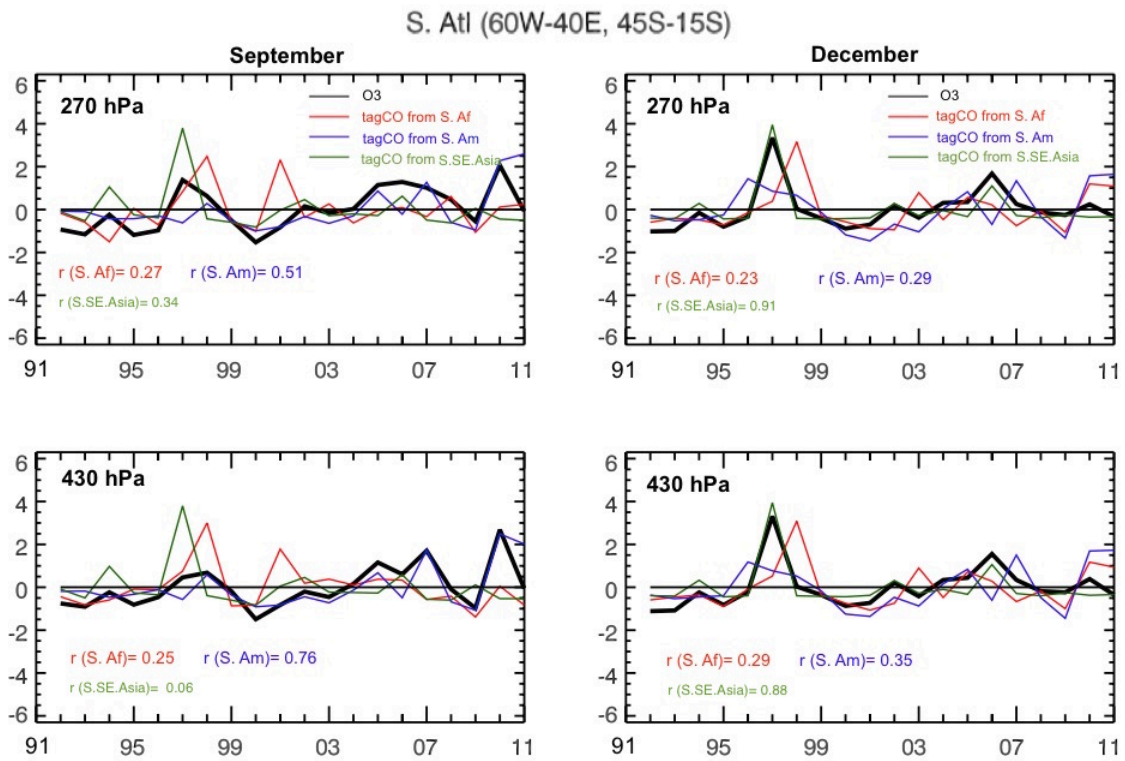
972

973

974

975

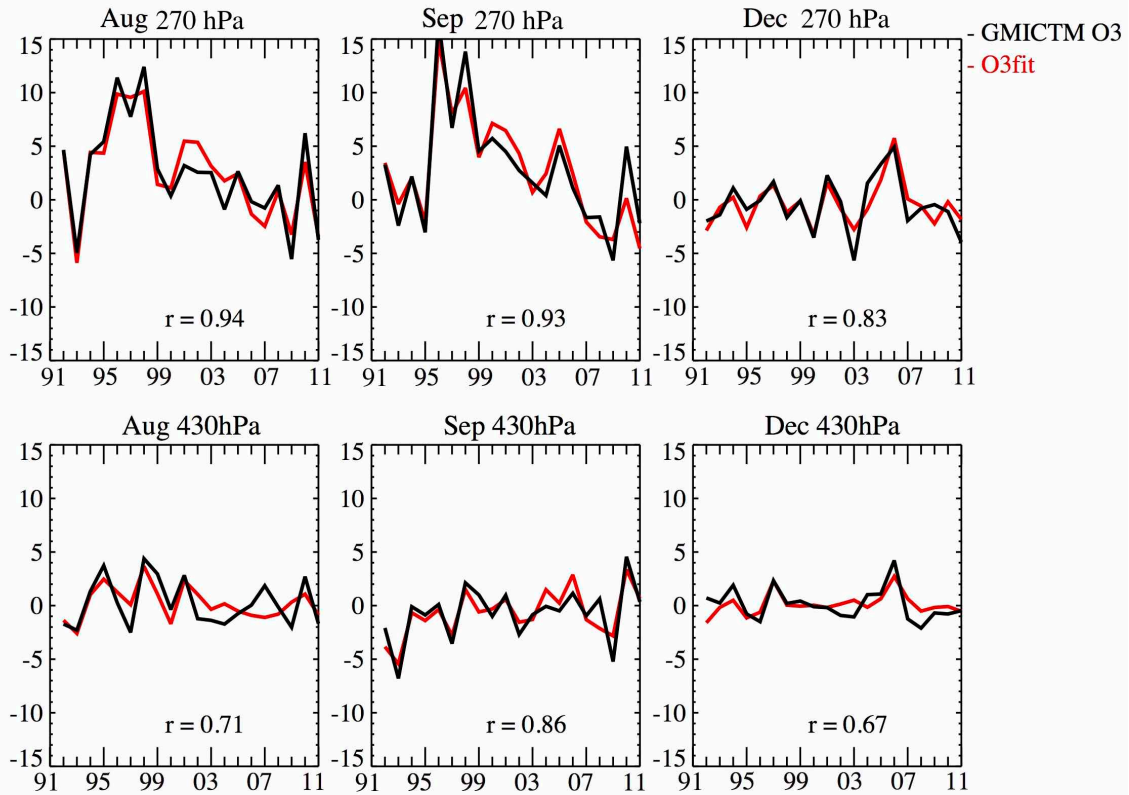
Figure 8: The multi-regression results of simulated ozone anomalies over South Atlantic region relying on two predictor variables: StratO₃ (blue), EmissO₃ (green) at 270 hPa and 430 hPa. Three panels show results from August (left), September (middle) and December (right) from 1992 to 2011. Each panel contains two columns. The left column of each panel compares the anomalies of StratO₃ (blue) and simulated ozone mixing ratio (black) from the GMI-CTM model at 270 and 430 hPa. The right column compares the simulated O₃ residual after removing the regression from StratO₃ (black line) and EmissO₃ (green line) at these two levels. EmissO₃ is calculated from the difference of simulated ozone between the run with yearly-varied emission and the run with constant emission. Unit for y-axis is ppb. The variance explained by each predictor (var), regression coefficient (β) and its 95% confidence level are labeled in each panel.



977
 978
 979
 980

Figure 9: The standardized anomalies of the tagged CO tracers over South Atlantic from three burning source regions, including southern Africa (red), South America (blue) and South and Southeast Asia (green) and their comparison with the EmissO₃ (black) at 270 and 430 hPa in September and December from 1992 to 2011.

S. Ind(40E-150E,45S-15S)



981

982

Figure 10: Comparison of the simulated ozone anomalies and the reconstructed ozone anomalies relying on two predictor variables: StratO₃, EmissO₃ at 270 hPa and 430 hPa over South Indian Ocean region. Three panels

983

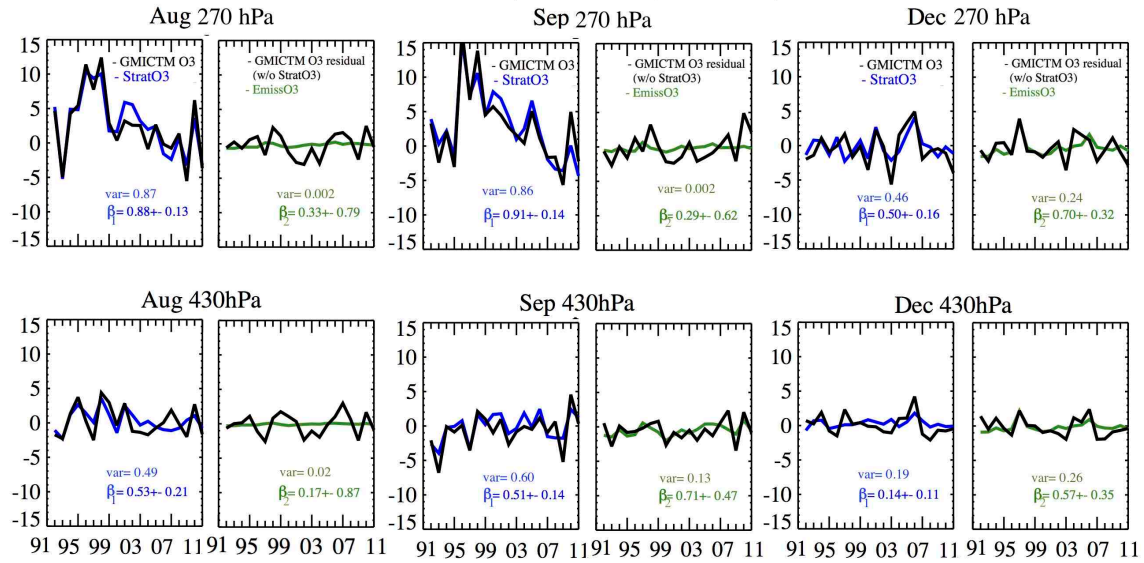
show results from August (left), September (middle) and December (right) from 1992 to 2011. Unit for y-axis is

984

ppb.

985

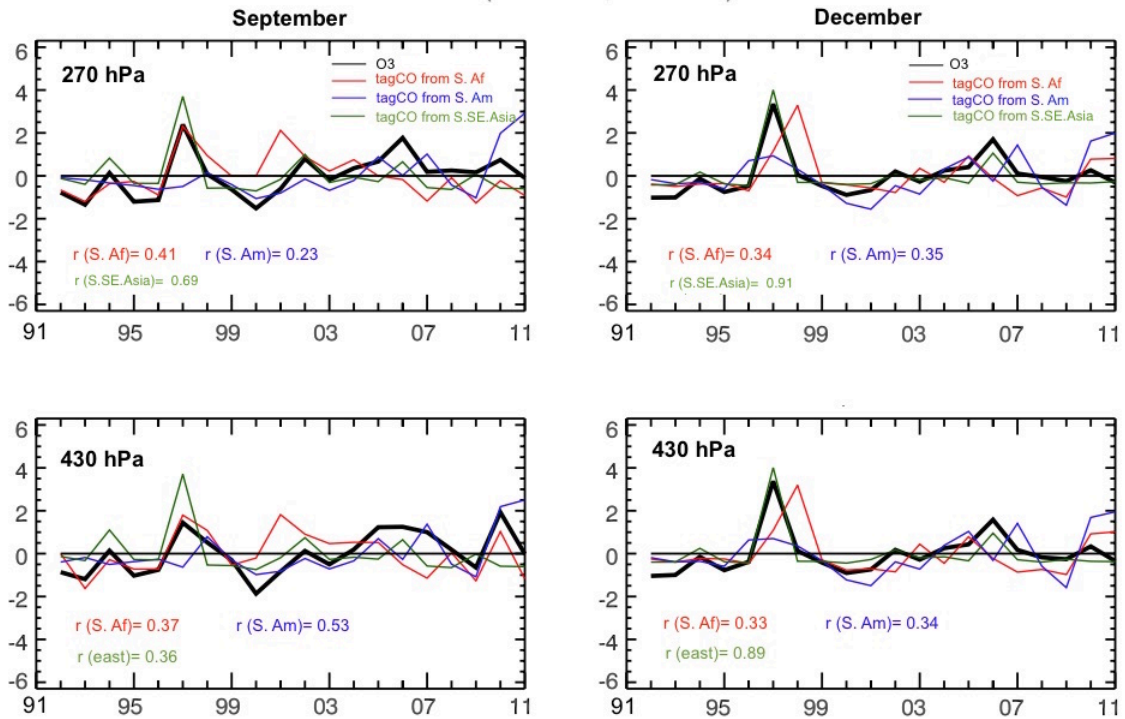
S. Ind(40E-150E,45S-15S)



986
987
988
989
990
991
992
993
994
995

Figure 11: The multi-regression results of simulated ozone anomalies over South Indian Ocean region relying on two predictor variables: StratO₃ (blue), EmissO₃ (green) at 270 hPa and 430 hPa. Three panels show results from August (left), September (middle) and December (right) from 1992 to 2011. Each panel contains two columns. The left column of each panel compares the anomalies of StratO₃ (blue) and simulated ozone mixing ratio (black) from the GMI-CTM model at 270 and 430 hPa. The right column compares the simulated O₃ residual after removing the regression from StratO₃ (black line) and EmissO₃ (green line) at these two levels. EmissO₃ is calculated from the difference of simulated ozone between the run with yearly-varied emission and the run with constant emission. Unit for y-axis is ppb. The variance explained by each predictor (var), regression coefficient (β) and its 95% confidence level are labeled in each panel.

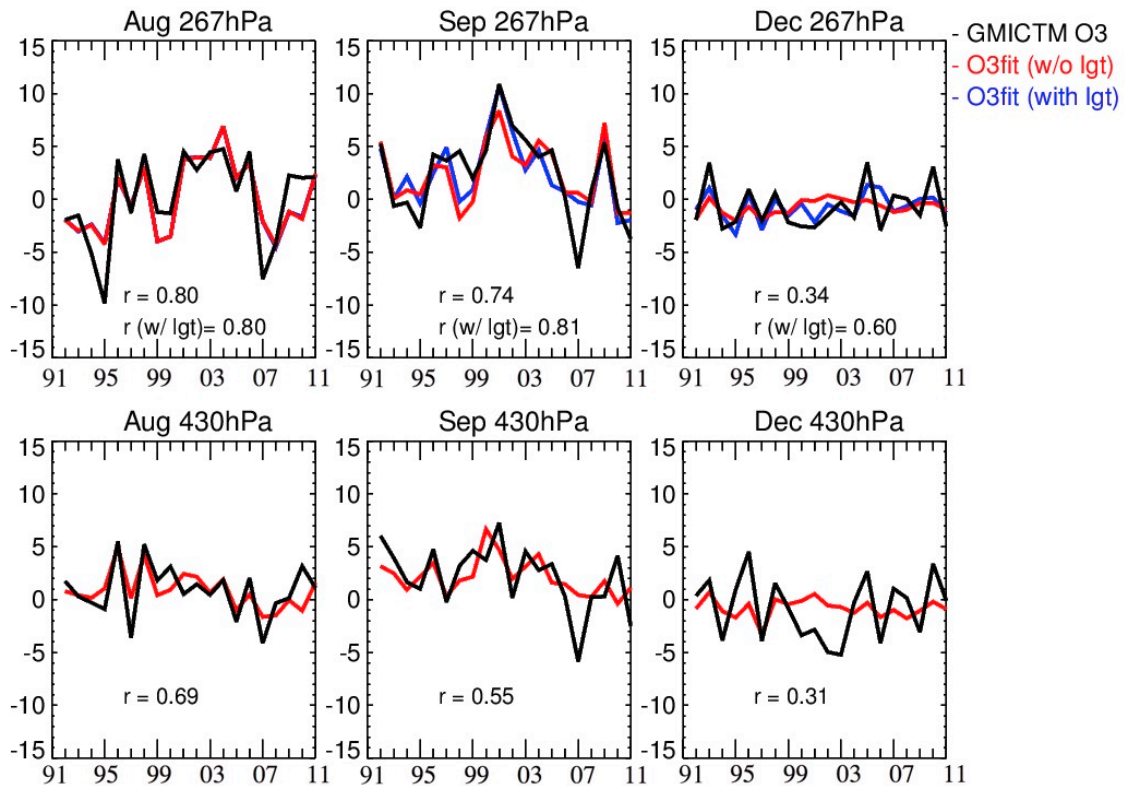
S. Ind(40E-150E,45S-15S)



997
 998
 999
 1000
 1001
 1002

Figure 12: The standardized anomalies of the tagged CO tracers over South Indian Ocean region from three burning source regions, including southern Africa (red), South America (blue) and South and Southeast Asia (green) and their comparison with the EmissO₃ (black) at 270 and 430 hPa in September and December from 1992 to 2011.

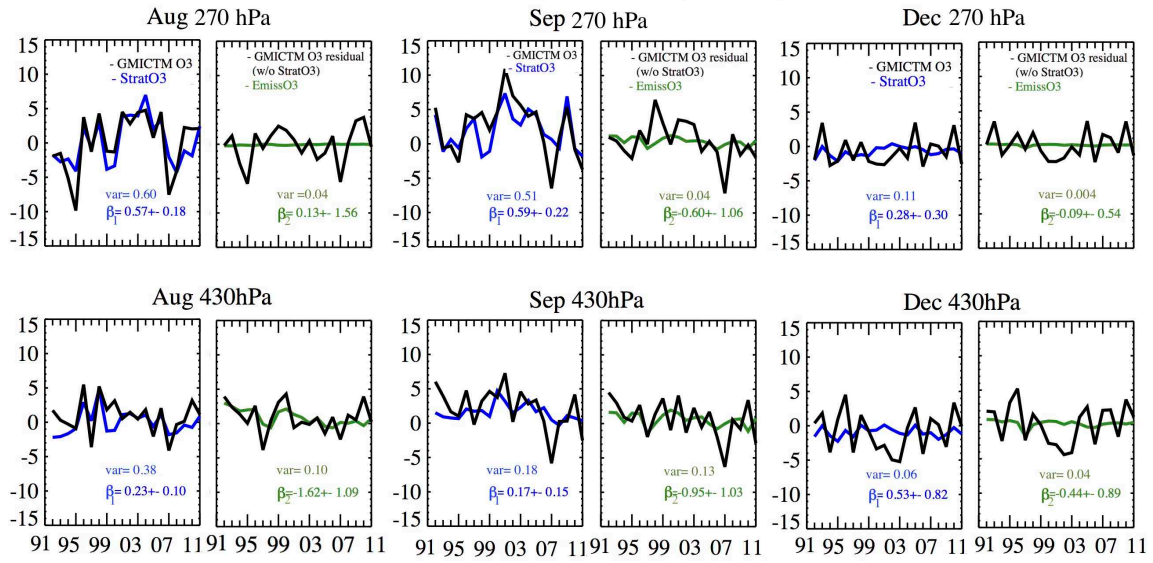
Tro. SATl (60W-40E, 0-15S)



1003
1004
1005
1006
1007
1008

Figure 13: Comparison of the simulated ozone anomalies and the reconstructed ozone anomalies relying on two predictor variables: StratO₃, EmissO₃ (red) over Tropical South Atlantic region at 270 hPa and 430 hPa. At 270 hPa, the reconstructed ozone anomalies from three predictor variables including lightning NO_x (blue) are added. Three panels show results from August (left), September (middle) and December (right) from 1992 to 2011. Unit for y-axis is ppb.

Tro SATl (60W-40E, 0-15S)



1009

1010

1011

1012

1013

1014

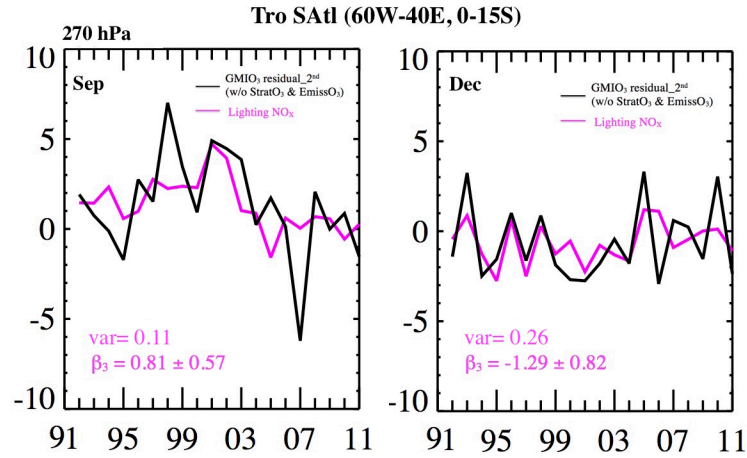
1015

1016

1017

1018

Figure 14: The multi-regression results of simulated ozone anomalies over tropical South Atlantic region relying on StratO₃ (blue), EmissO₃ (green) at 270 hPa and 430 hPa. Three panels show results from August (left), September (middle) and December (right) from 1992 to 2011. Each panel contains two columns. The left column of each panel compares the anomalies of StratO₃ (blue) and simulated ozone mixing ratio (black) from the GMICTM model at 270 and 430 hPa. The right column compares the simulated O₃ residual after removing the regression from StratO₃ (black line) and EmissO₃ (green line) at these two levels. EmissO₃ is calculated from the difference of simulated ozone between the run with yearly-varied emission and the run with constant emission. Unit for y-axis is ppb. The variance explained by each predictor (var), regression coefficient (β) and its 95% confidence level are labeled in each panel



1020

1021

1022

1023

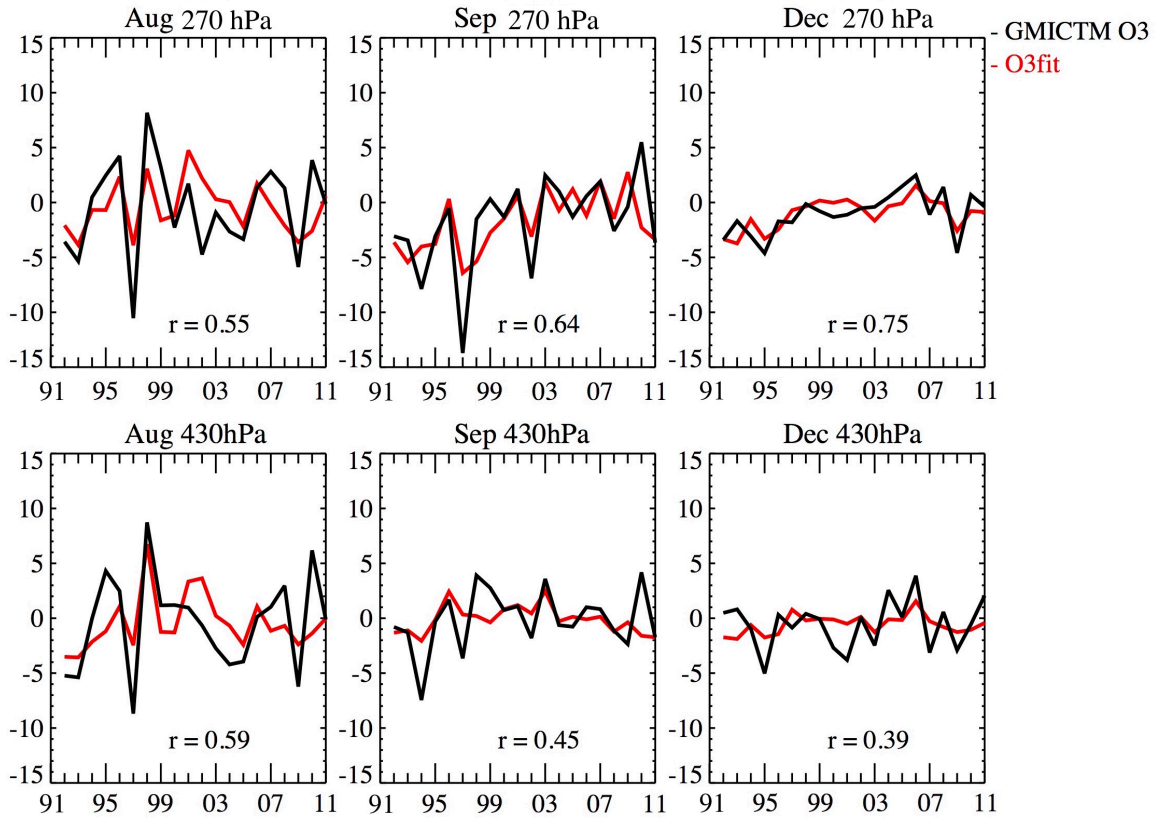
1024

1025

1026

Figure 15: The comparison between regression of lightning NO_x (magenta) and the ozone residual after removing the regression of StratO_3 and EmissO_3 (black) at 270 hPa in September (left) and December (right) over tropical South Atlantic region. The increased variance explained by the regression by adding lightning NO_x (var), regression coefficient (β) and its 95% confidence level are labeled in each panel.

Tro SEPaC (150W-60W, 0-20S)



1027

1028

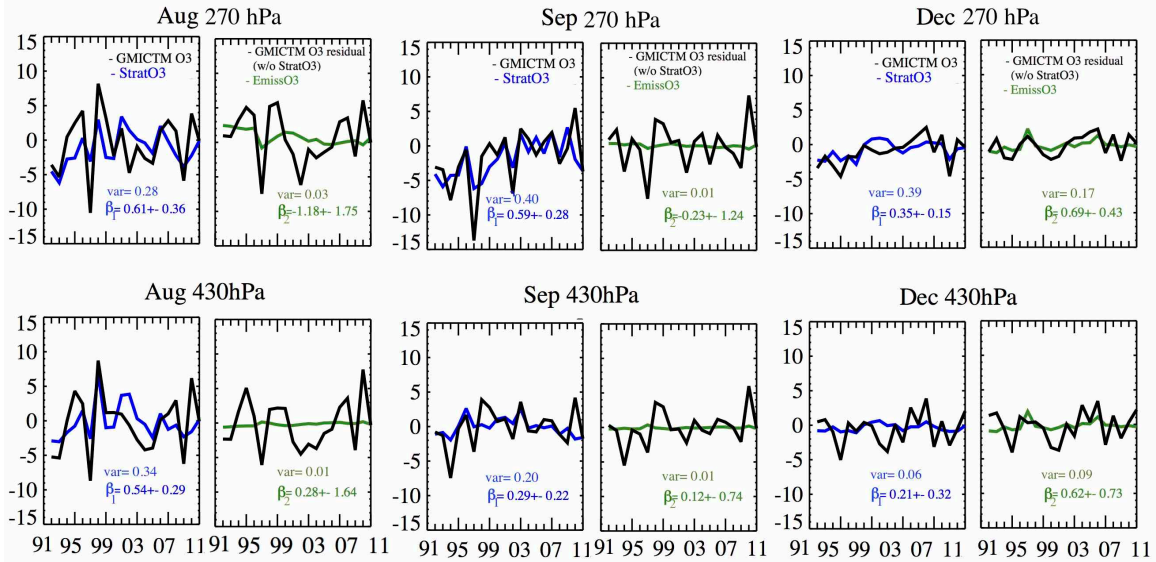
1029

1030

1031

Figure 16: Comparison of the simulated ozone anomalies and the reconstructed ozone anomalies relying on two predictor variables: StratO₃, EmissO₃ at 270 hPa and 430 hPa over Tropical southeastern Pacific. Three panels show results from August (left), September (middle) and December (right) from 1992 to 2011. Unit for y-axis is ppb.

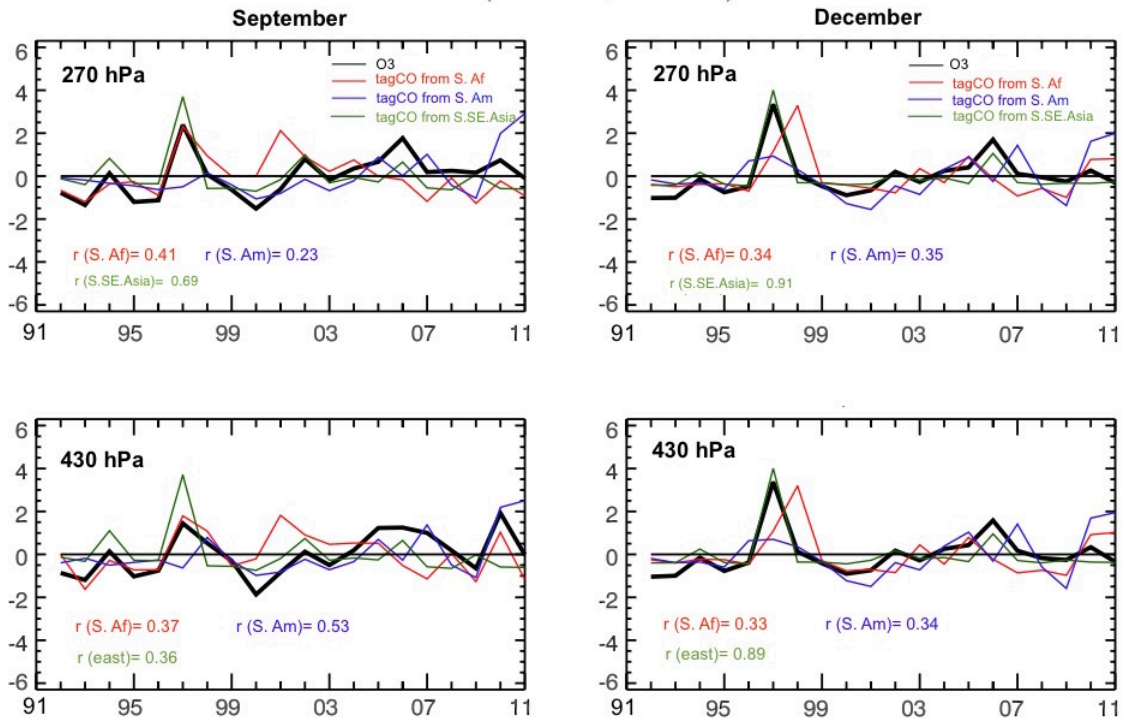
Tro SEpac (150W-60W, 0-20S)



1032
1033
1034
1035
1036
1037
1038
1039
1040
1041

Figure 17: The multi-regression results of simulated ozone anomalies over tropical southeastern Pacific region relying on two predictor variables: StratO₃ (blue), EmissO₃ (green) at 270 hPa and 430 hPa. Three panels show results from August (left), September (middle) and December (right) from 1992 to 2011. Each panel contains two columns. The left column of each panel compares the anomalies of StratO₃ (blue) and simulated ozone mixing ratio (black) from the GMI-CTM model at 270 and 430 hPa. The right column compares the simulated O₃ residual after removing the regression from StratO₃ (black line) and EmissO₃ (green line) at these two levels. EmissO₃ is calculated from the difference of simulated ozone between the run with yearly-varied emission and the run with constant emission. Unit for y-axis is ppb. The variance explained by each predictor (var), regression coefficient (β) and its 95% confidence level are labeled in each panel.

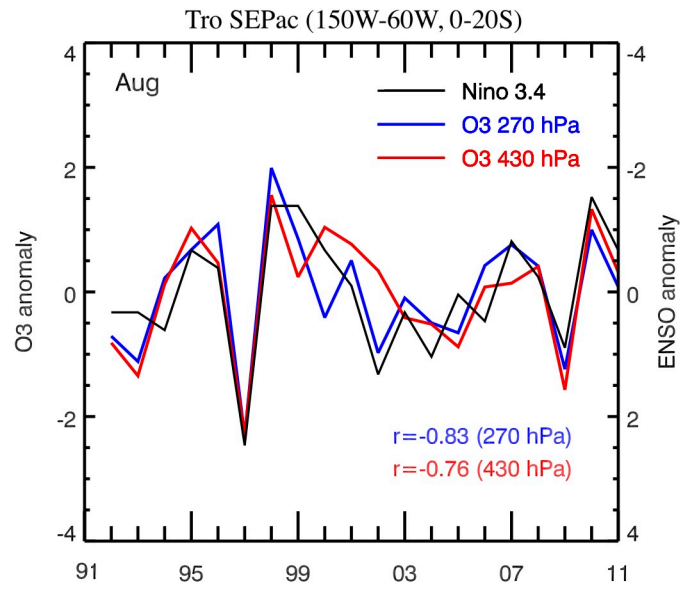
S. Ind(40E-150E,45S-15S)



1042
1043
1044
1045
1046
1047

Figure 18: The standardized anomalies of the tagged CO tracers over tropical southeastern Pacific region from three burning regions, including southern Africa (red), South America (blue) and South and Southeast Asia (green) and their comparison with the EmissO3 (black) at 270 and 430 hPa in September from 1992 to 2011.

1048
1049



1050
1051 **Figure 19: Comparison of IAV of ozone anomalies over tropical southeastern Pacific region at 270 hPa (blue)**
1052 **and 430 hPa (red) with Niño 3.4 index in August from 1992 to 2011. The 2nd y-axis for the ENSO anomaly is**
1053 **reversed.**
1054